Journal of Petroleum Science and Engineering 208 (2022) 109346

Contents lists available at ScienceDirect

Journal of Petroleum Science and Engineering

journal homepage: www.elsevier.com/locate/petrol

# An integrated fracture parameter prediction and characterization method in deeply-buried carbonate reservoirs based on deep neural network

Qamar Yasin [a,*], Yan Ding [b], Syrine Baklouti [c], Cyril D. Boateng [a], Qizhen Du [a,**], Naser Golsanami [d,e]

[a] The Key Laboratory of Deep Oil and Gas, China University of Petroleum (East China), Changjiang West Road 66th, Qingdao, 266580, China
[b] CNPC Engineering Technology R&D Company Limited, Beijing, 102206, China
[c] Department of Geological and Environmental Engineering, National School of Engineers of Sfax, Tunisia
[d] State Key Laboratory of Mining Disaster Prevention and Control, Shandong University of Science and Technology, Qingdao, 266590, China
[e] College of Energy and Mining Engineering, Shandong University of Science and Technology, Qingdao, 266590, China

ARTICLE INFO

*Keywords:*
Deep-learning neural network
Seismic inversion
Petrophysical modeling
Fracture prediction
Buried-hill

ABSTRACT

Deeply buried fractured reservoirs have evolved into significant oil and gas potential in many basins of the world. However, fracture prediction in deeply buried carbonate reservoirs has always been challenging. Fracture prediction in the deep-buried carbonate structure of North China is problematic because of multiphase tectonic movements, variable sediment lithology, and complex diagenesis. Because of deep burial depth and complex heterogeneity, the resolution of seismic reflection data beneath the buried-structure is poor, making it challenging to identify the fault reflection characteristics. This paper proposes a novel idea to identify natural fractures in carbonate reservoirs using conventional logs with seismic reflection data. The proposed model can also predict the fracture aperture and fracture density, a distinctive feature. Another novel hybrid model based on deep-learning neural network (DNN) and cluster analysis is proposed to predict further the spatial variations of lithology, porosity, and fracture parameters from seismic inversion. The proposed models provide valuable insights that help determine fracture parameters in the Paleozoic strata and associated reservoirs through quantitative analysis using petrophysics, rock physics, seismic inversion, and seismic attributes. The overlapping of seismic interpreted fault networks and spatial variations of the inverted fracture parameters indicate a high correlation of fracture development zones. The methodology proposed in this study presents a valuable template valid for the characterization of fractured reservoirs in deeply-buried carbonate reservoirs throughout the world.

## 1. Introduction

Naturally fractured carbonate reservoirs have contributed significantly to petroleum reserves after recent significant advances in geosciences (Aghli et al., 2016; Aguilera, 2010; Ginting et al., 2011; Yasin et al., 2018a). However, the correct identification of the fractures´ distribution in deeply-buried reservoirs is still challenging and has become an obstacle for seismic interpreters to explore the fractured reservoirs (DING et al., 2020; Saboorian-Jooybari et al., 2015). Conventionally, geologists and geophysicists use cores, and formation micro-imaging (FMI) logs for fracture evaluation (Tao and Alves, 2019). FMI logs can be used directly to determine fracture parameters like aperture, orientation, and porosity (Khoshbakht et al., 2012). However, these tools are costly and are rarely available in all wells (Ferrill et al., 2017; Tokhmchi et al., 2010).

Over the past decade, significant progress has been made in the development of digital outcrop models (DOM) for fracture characterization (Casini et al., 2016; Larssen, 2018), mapping of sedimentary and igneous bodies (Galland et al., 2019), and as input for seismic modeling. The fracture systems from outcrops are investigated using Lidar scanning, photogrammetry, and satellite photos (Hodgetts et al., 2004; Smith et al., 2015). Photogrammetry-based DOM is the most popular method for acquiring outcrop images, as it only requires a camera and processing software. It is helpful in various geological settings, but it is especially useful for characterizing extremely heterogeneous carbonate platforms (Loza Espejel et al., 2020).

* Corresponding author.
** Corresponding author.
*E-mail addresses:* qamarquaidian@gmail.com (Q. Yasin), syrine.baklouti.mtibaa@gmail.com (S. Baklouti), multicomponent@163.com (Q. Du).

https://doi.org/10.1016/j.petrol.2021.109346
Received 15 February 2021; Received in revised form 16 July 2021; Accepted 5 August 2021
Available online 9 August 2021

While those techniques are designed only for outcrops, alternative tools based on conventional logs have recently been proposed to investigate the fractures´ distribution. In fact, fractures contribute directly to the porosity of the reservoir, and hence the conventional porosity logs are strongly related to fracture parameters as fracture aperture (Ouenes, 2000; Ouenes et al., 1995). The fracture aperture also provides a vital contribution to the rock permeability, i.e., the larger the aperture size, the more fluid phases can flow in the fracture (Aguilera, 2010; Al-Ghamdi et al., 2010; Movahed Z., 2015). To understand the fractured reservoir's behavior, we should perform estimations for both the primary (matrix) and secondary (fracture-only) porosities (Hornby et al., 1992; Mohebbi et al., 2007; Ouenes, 2000). However, porosity formed by fractures is considered too small to detect with conventional logs due to their low vertical resolution (Hornby et al., 1992; Mohebbi et al., 2007). Recent studies have shown that fracture zones can be identified on conventional logs while modern logging tools are being designed specially to provide higher resolution (Aghli et al., 2016, 2019; Ge et al., 2014; Tokhmchi et al., 2010; Tokhmechi et al., 2009). The researchers have recognized sonic, density, resistivity, gamma-ray (uranium), neutron porosity, and caliper logs as the best logging combination for fracture identification (Ge et al., 2014; Martinez et al., 2002; Saboorian-Jooybari et al., 2015).

P-wave and S-wave (e.g., compressional and shear sonic logs) indicate the formation's interval transit time (Du et al., 2018, 2019). (Wyllie et al., 1956) proposed the relationships between acoustic travel time versus porosity, and since then, the oldest and most popular Wyllie time-average is considered the most common equation for the field. The transmission speed in the fractured zone is reduced due to the formation's low density (especially in open fractures). Based on this, we expect transit time to increase in the fractured zones (Aghli et al., 2019; Golsanami et al., 2021).

Neutron log (e.g., porosity or NPHI) measures hydrogen concentration in a formation and determines porosity. Hydrocarbons and water are organic molecules consisting of large amounts of hydrogen that significantly reduce the neutron speed. High hydrogen concentrations in the pore network system result in neutron energy loss, reflecting the formation porosity (Ismail et al., 2017; Laongsakul and Dürrast, 2011). Therefore, in the fracture zones, where there is an increase in the amount of formation fluid, there is a corresponding increase in the neutron log values. Hence, the neutron log could be the best log for the prediction of fracture aperture.

Shallow and deep resistivity logs (LLS and LLD) are also suitable for fracture detection among old and new logging measurements. The shallow resistivity curve shows lower values along with the fracture intervals because of fluid invasion in the fractures, especially when the true resistivity of the formation is greater than the resistivity of mud (Saboorian-Jooybari et al., 2015). Similarly, the induction log shows low resistivity spikes on resistivity curves that indicate the presence of fractures (Golsanami et al., 2020). If deeper induction resistivity curves show spikes to lower resistivity, we suppose that the pre-existing fractures are quite deep and also significant (Bakhshi et al., 2020; Golsanami et al., 2019).

Moreover, the microfractures are generally filled with uranium minerals which are commonly determined by spectral gamma-ray logs (SGR). Petrophysicists use SGR to estimate clay mineral volumes and identify fractures containing uranium salts precipitated in there by ground-water systems (Aghli et al., 2019; Darling, 2005).

The bulk-density (RHOB) log is also significantly influenced by the fracture zones. Previous studies indicate that the density curve shows a significant difference between the rock and fluid density around the fracture zones (Laongsakul and Dürrast, 2011; Saboorian-Jooybari et al., 2015; Yasin* et al., 2020b). An increase in fluid volume in fractured zones leads to density contrast because fluid density is less than rock density (Yasin et al., 2018b).

Besides all the above conventional logs used for simple fracture prediction, progress in high-performance computing systems has enabled data-driven machine learning (ML) algorithms to establish the nonlinear relationships between two variables (input and output) based on a statistical approach (Al Moqbel and Wang, 2011; Dandan and Qiaodeng, 2002; Qiang et al., 2020; Russell, 1988, 2004). Geoscientists have recently succeeded in applying intelligent ML algorithms to high-quality seismic reservoir characterization. (Esmaeilzadeh et al., 2019, 2020). (Jun et al., 2006) established the mapping relationship between logging porosity and seismic multi-attributes with the conventional NN method to predict fracture development zones in carbonate reservoirs (Lin et al., 2018). used a combination of the soft-porous petrophysics model and conventional NN to calculate fracture porosity and then used formation micro-image (FMI) logging to confirm the accuracy of the fracture prediction (Luo et al., 2021). recently proposed a parametrized residual rock physics model for reliable production data forecasts using machine learning methods. Although various ML algorithms have been proposed for seismic inversion, e.g., back-propagation (BP), support vector machine (SVM), genetic inversion, particle swarm optimization (PSO), and multi-layer linear calculator (Abdulaziz et al., 2019; Boateng et al., 2020; Nwachukwu et al., 2018; Yasin et al., 2020a; Zhang and Ruan, 2009), the practical use of the suitable inversion algorithm is still a challenging task and depends a lot on the quality of input data and stage of exploration or field development.

In recent decades, substantial development has been made in deep-learning neural networks (DNN) to improve the spatial prediction of petrophysical, geological, and geomechanical properties in conventional and unconventional reservoirs (Hinton et al., 2006; Lin et al., 2018; Wu and Cao, 2016). Deep learning's core idea is to learn the nonlinear relationship between inputs and outputs, as well as the underlying structure of data vectors. In contrast to the single-layer neural network, a DNN contains many hidden layers with strong learning abilities to improve prediction accuracy (Temirchev et al., 2020). It is composed of a multi-layer processing structure that can divide a complex function into many simple linear functions by controlling each layer's output weight (Lin et al., 2018). The structure of DNN is more complex and represents the learning mode of big data plus a complex model. It is a semi-supervised generation model, i.e., the training of DNN needs to be carried out in two steps by way of unsupervised and supervised neural networks. In the first step, the weights of each neuron are trained in an unsupervised manner. The whole neural network generates data according to the maximum probability to form clustering information. In the second step, BP is used to guide the DNN to fine-tune network parameters, that is, to optimize with a supervised neural network (Lin et al., 2018).

The DNN is appropriate for complex and highly fractured reservoirs, such as the buried-hill carbonate reservoir in the oilfield X, one of the largest oilfields in North China. The geological reserves of the buried-hill are nearly 200 million tons (Sun et al., 2018). It is a regional oil and gas-bearing area with 65 oil and gas fields, two gas fields, and eight major oil fields covering about 2117 $km^2$. The multiphase tectonic movements, complex diagenesis, well-developed faults network, and low-frequency seismic reflection data cause extreme heterogeneity. Consequently, an accurate description of the fault network, fracture development zone, lithology, and reservoir parameters, to identify high-quality reservoir regions of the deeply-buried structure; is a challenging task in this area. This study proposes a novel, inexpensive, and reliable method based on the combination of high-resolution conventional logs with seismic data. This method consists of a meticulous application of various tools for evaluating the fracture parameters. Herein, we explore the relationship between fracture-sensitive parameters and the reservoir rock's elastic properties to define the fractured and non-fractured zones. Also, we suggest the DNN inversion strategy to predict spatial variations of lithology, porosity, and fracture parameters using 3D seismic reflection data. The present study's proposed methodology would effectively acquire the fractured zone's most subtle information from the low-frequency seismic data and conventional logs,

contributing to the more profound understanding of the petrophysical characteristics of the subject's buried-hill structure.

## 2. Geological setting and stratigraphy

The study area is located in the North China of Y Basin. Tectonically, it is subdivided into depressions and uplifts, roughly oriented NE-SW by transtensional faults which are themselves compartmentalized into sub-units ('sags' and 'rises') (Cai et al., 2008). Regarding the regional framework, the oilfield lies in the northeast part of the Zhuangxi-Gudong buried-hill anticlinal belt of the Zhanhua sag. It is adjacent to the Kendong-Qingtuozi dome in the SE, the Gunan sag in the SW, the Zhuangxi sag in the NW, and the Zhuangdong sag in the NE (Fig. 1a) (Cai et al., 2008; Sun et al., 2018; Yue, 2007). The Zhanhua sag comprises a basement fault block pattern, which is faulted in the southern part and overlapped in the northern part. The sag exhibits a NE trend and 'double half-graben' structure in the planar view. The structural features are affected mainly by the tensional and transtensional faults of NE directions (Yue, 2007).

Stratigraphically, the oilfield X is a large anticlinal buried-hill structure developed from the Paleozoic stratum. Lithologies are mainly primarily oolitic limestone and dolomite with many high angle fractures (Fig. 1b). These limestones and dolomite of the Paleozoic formations act as the main reservoir unit in the buried-hill structure. The limestone section is mainly fractured and filled with calcite. At the bottom intervals, the limestone and dolomite section comprises breccia, calcite filling, and argillaceous filling. The breccia of fractured limestone and dolomite intervals are filled with oil (Fig. 1b). (DING et al., 2020) recently applied deep neural networks to predict fractures' spatial distribution in the Paleozoic formations' buried-hill structure. In the same oilfield, they discovered a well-developed northeast trending fracture network along the fault.

Subsurface well correlation indicates that the Paleozoic strata under the buried-hill were eroded to a large extent. The thinnest eroded strata were at the top, compared with the regular sections. Towards the northern direction, the eroded thickness of strata is high. Meanwhile, the lower Paleozoic strata are seriously faulted, relatively thin, with rapid lateral horizon variation. The lower Paleozoic strata encountered in several wells are different, and the horizontal and vertical distribution is also unstable (Fig. 2).

Boundary faults principally control the whole structure. There are mainly two normal extensional faults at the boundary of the buried-hill. Simultaneously, there are two large secondary NE faults, i.e., the fault south of the 30A-2 well and the fault north of the 301 well. These faults make the buried hills' central fault system more complicated and control its structure. The faults along the EW direction also play a significant role in forming the structure and trapping the hydrocarbons. Note that each block has different structural characteristics to trap the oil and gas accumulation, which complicates more and more the exploration.

## 3. Dataset and methodology

This study used borehole log data from more than ten producing wells to estimate fracture parameters and reservoir properties in the lower Paleozoic (Pz) interval. We analyzed caliper (CAL), gamma-ray (GR), deep resistivity (LLD), spontaneous potential (SP), P- and S-wave sonic (DTP and DTS), density (RHOB), and neutron porosity (NPHI) log to explore the fracture zones for reservoir modeling from the following key wells: 302, 306, 307, 39, 40, 313, and 30. Also, several thin sections were available in the reservoir interval to calibrate porosity and fractures. Furthermore, we utilized 3D seismic data covering about 200 $km^2$ to interpret the target horizons, i.e., 'Pz' (lower Paleozoic) interval top and 'Art' (igneous rock) top for reservoir characterization and modeling.

The following is a detailed description and overview of a specific workflow proposed to analyze fracture parameters using a combination of high-resolution conventional logs and seismic reflection data (Fig. 3).

a) A theoretical model based on unique logging response versus fractures was developed to predict fracture parameters.
b) A hybrid model based on deep-learning neural network and cluster analysis was proposed to measure the spatial variations of lithology, porosity, and fracture parameters using seismic data.
c) The results were compared by overlapping the seismic interpreted fault network and spatial variations of the inverted AI, lithofacies, and fracture parameters.

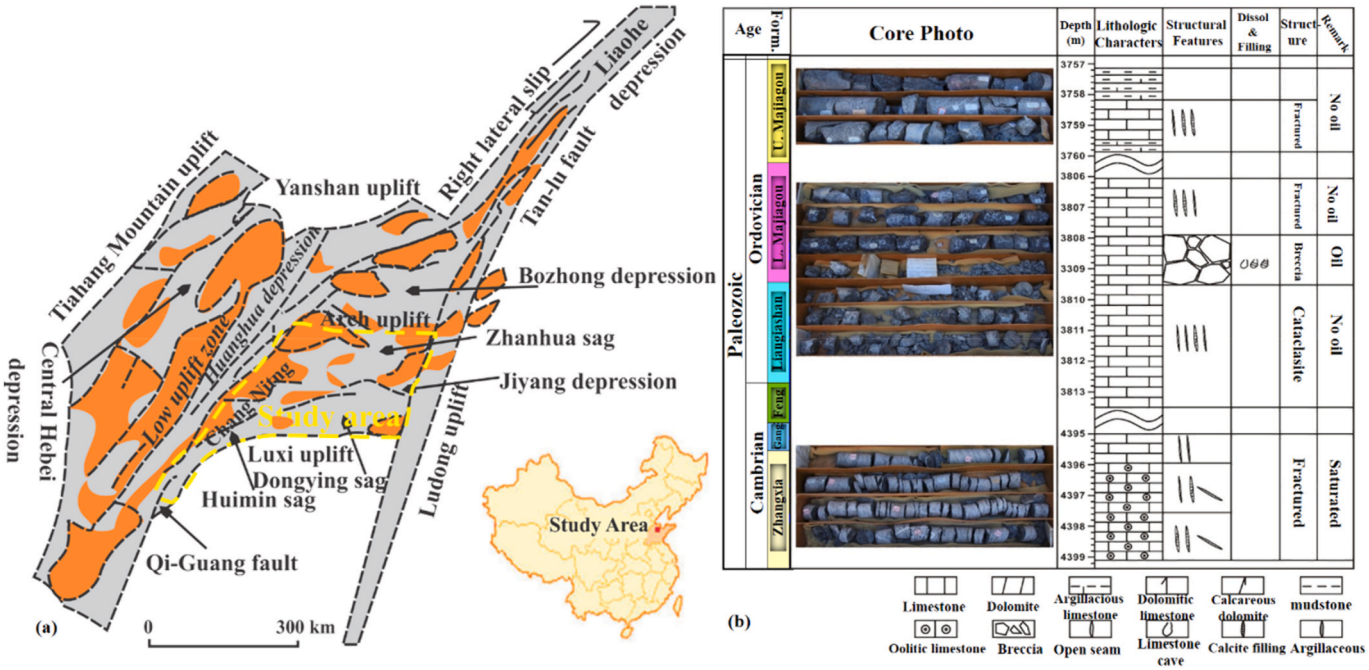


**Fig. 1.** (a) Regional tectonic framework of the study area (modified after (Sun et al., 2018), (b) identification of structural features and lithologic characteristics from the cores of the studied interval.

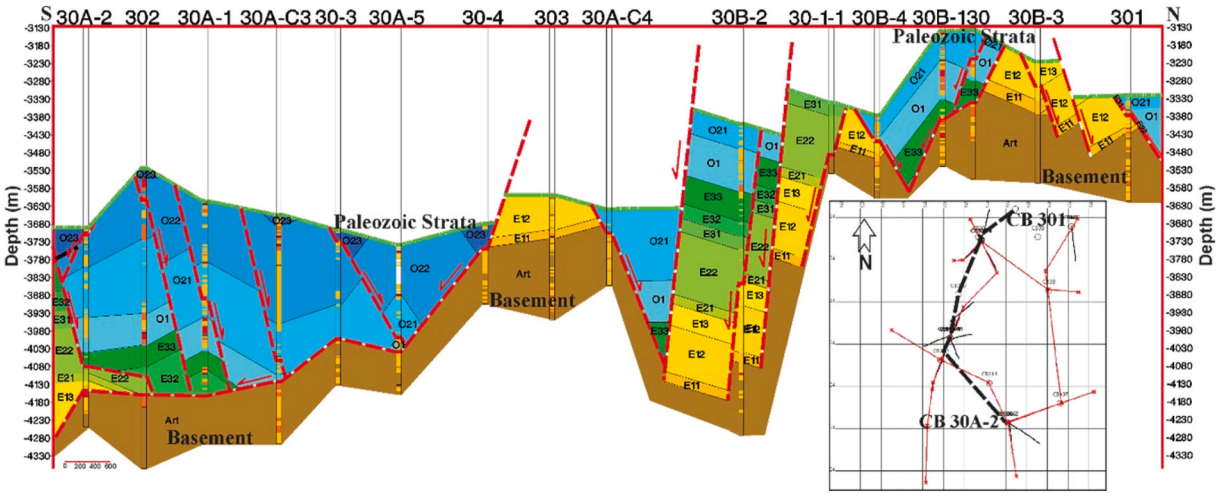


**Fig. 2.** Stratigraphic sequences and structural architecture in the buried-hill. Note that O21, O22, O1, E33, E32, E31, E22, E21, E13, E12, and E18 are members of the Paleozoic strata, and 'Art' stands for basement rocks.

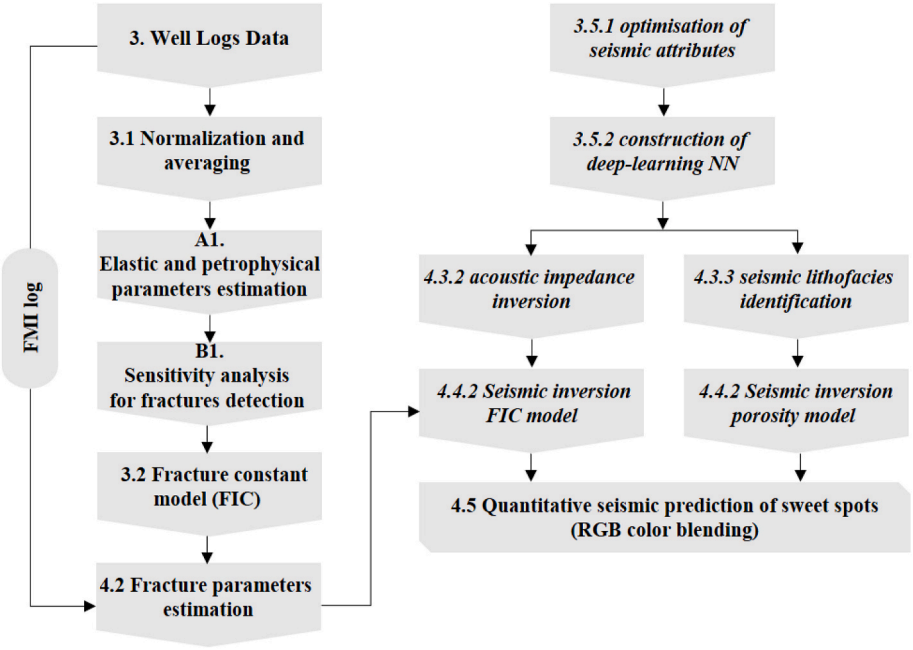


**Fig. 3.** Proposed workflow for fracture parameters estimation.

d) The RGB color blending visualization was used to assess the quantitative seismic prediction of sweet spots.

### 3.1. Logs´ data normalization and averaging

Delineating fracture patterns from log data is an intricate process that classical regression techniques cannot evaluate. Therefore, the log's pre-processing is considered an essential step before evaluating fractures. We performed initial processes such as averaging and normalizing the raw petrophysical logs to get an equal contribution from all types of logs. Without data normalization, the GR and DT logs would dominate in the process steps. We normalized the input logs using $X_{\min}$ and $X_{\max}$ by Eq. (1). Also, we used cross-correlation to evaluate the similarity between two signals, i.e., comparing and analyzing the logs and fracture parameters before and after applying log's processing. Cross-correlation of the logs and fracture parameters was normalized as 'logs' data per energy for each log.

The normalized data was measured by Eq. (2) and Eq. (3).

$$X_{Norm} = \frac{X_i - X_{\min}}{X_{\max} - X_{\min}} \tag{1}$$

$$E_{\log} = \sum_{i=1}^{n} X_i^2 \tag{2}$$

$$N_{\log} = \frac{X_i}{\sqrt{E_{\log}}} \tag{3}$$

where '$i$' indicates the index of the data points on each individual log, and $E_{log}$ and $N_{log}$ denote each log's total energy and normalized log per energy, respectively.

Averaging the petrophysical logs is another preferred method for increasing the relationship between input and output variables. It is a statistical procedure that relies heavily on the resolution of each log. The

averaging range varies between 50 and 200 data points, e.g., depending on the log's resolution (Eq. (4)). The averaging range of a log with 0.15 cm resolution is 50, e.g., DT. A log with a resolution of 0.05 cm, on the other hand, has a range of averaging of 200, e.g., LLD. Notice that 'c' is a constant weight factor (between 0 and 1) that is highly dependent on the resolution of each log (Eq. (4)). Instead of a single point, log averaging shows the behavior of each log in an interval (Luo et al., 2016).

$$X_{int} = \frac{X_i + (1+c)a_{(i)}}{2+c}, 0 < c \leq 1 \tag{4}$$

$$a(i) = \left\{ \begin{array}{l} \dfrac{\sum_{k=i}^{i+50} dt(k)}{50}, i < 51 \\ \dfrac{\sum_{k=i-50}^{i+50} dt(k)}{100}, 51 < i < 6261 \\ \dfrac{\sum_{k=i-50}^{i} dt(k)}{50}, 6261 < i < 6311 \end{array} \right\} \text{When log resolution is 0.15 and c is 0.1} \tag{5}$$

$$a(i) = \left\{ \begin{array}{l} \dfrac{\sum_{k=i}^{i+200} gr(k)}{200}, i < 201 \\ \dfrac{\sum_{k=i-200}^{i+200} gr(k)}{100}, 201 < i < 6111 \\ \dfrac{\sum_{k=i-200}^{i} gr(k)}{200}, 6111 < i < 6311 \end{array} \right\} \text{When log resolution is 0.05 and c is 0.2} \tag{6}$$

where '*dt*' and '*gr*' stand for sonic and gamma-ray logs, respectively, and '$X_{int}$' and $X_i$ signify log readings in a specific interval. Note that '$a_{(i)}$' is the number of nth point data before and after $X_i$, and 1+ c is vertical resolution weight factor.

### 3.2. Fracture identification constant (FIC) model prediction

According to recent studies, fractures influence significantly conventional well logs (Aghli et al., 2016; Mohebbi et al., 2007; Tokhmchi et al., 2010). According to researchers, a single conventional log might not distinguish fracture zones, but a combination of conventional logs is useful (Ge et al., 2014; Martinez et al., 2002; Saboorian-Jooybari et al., 2015). We developed a theoretical model based on unique logging response versus fractures by combining gamma-ray (uranium content), shallow and deep resistivity (RD and RS), compressional and shear sonic (DTP, DTS), density (DEN), and neutron porosity (CNL) logs (Eq. (7) to (11)). However, it is important to note that certain logs show defiant behavior and cancel one another. To avoid this, we convert the model's parameters into positive factors. Furthermore, we normalize the factors between 0′ and 1′ in order for each log to participate equally in the model development process. As shown in Eq. (12), the combined effect of all normalized logs is referred to as the fracture identification constant (FIC) model. Note that the reservoir interval was divided into homogeneous subgroups based on mineralogy, rock type, facies, and pore fluid for reliable fracture prediction.

$$A = (GR - Average)^2 \Rightarrow A_n = \sum_{i=1}^{n} \left( \frac{A - A_{min}}{A_{max} - A_{min}} \right)_{zone\ i} \tag{7}$$

$$B = (RD - RS)^2 \Rightarrow B_n = \sum_{i=1}^{n} \left( \frac{B - B_{min}}{B_{max} - B_{min}} \right)_{zone\ i} \tag{8}$$

$$C = (CNL - Average)^2 \Rightarrow C_n = \sum_{i=1}^{n} \left( \frac{C - C_{min}}{C_{max} - C_{min}} \right)_{zone\ i} \tag{9}$$

$$D = (DTP - DTS)^2 \Rightarrow D_n = \sum_{i=1}^{n} \left( \frac{D - D_{min}}{D_{max} - D_{min}} \right)_{zone\ i} \tag{10}$$

$$E = (Average - DEN)^2 \Rightarrow E_n = \sum_{i=1}^{n} \left( \frac{E - E_{min}}{E_{max} - E_{min}} \right)_{zone\ i} \tag{11}$$

$$FIC = A_n + B_n + C_n + D_n + E_n \tag{12}$$

where GR = gamma-ray, DEN = density, RD = resistivity deep, RS = resistivity shallow, DTP = compressional sonic, DTS = shear sonic.

### 3.3. Well-to-seismic calibration

Seismic inversion is the process of converting seismic reflection data into reservoir physical properties. The process of generating and calibrating synthetics seismogram to real field seismic data is an art. The first move in calibrating well-to-seismic is to use seismic data to calibrate sonic (acoustic) and bulk density logs. In this workflow, 3D seismic volume, acoustic, and bulk density logs were imported into the open-source rock star seismic inversion software (Beijing Rock Star Petroleum Technology Co. Ltd.). We extracted the wavelet directly from the seismic dataset, i.e., seismic traces from inline and crossline with the evaluation window ranges from 2100 to 2800 ms. To generate a

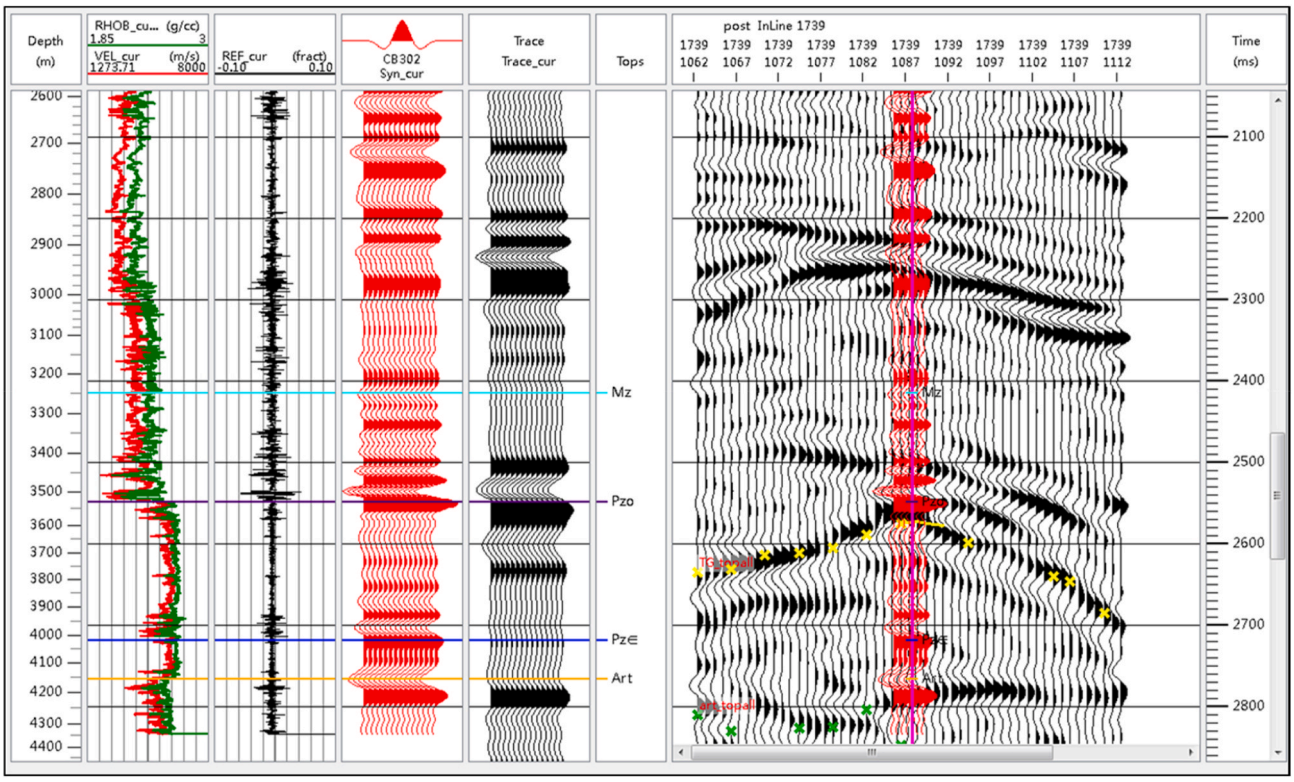


**Fig. 4.** Composite plot for the well 302 showing synthetic seismogram, reflectivity series, and extracted wavelet.

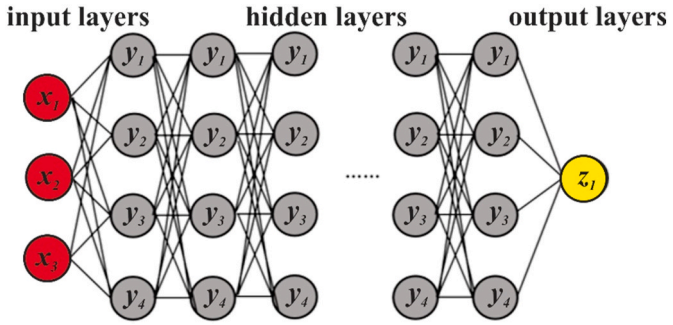


**Fig. 5.** A schematic representation of the DNN model. The input variables (seismic attributes) in the model are denoted by $x_1$, $x_2$, and $x_3$. The $y_1$ to $y_4$ shows the number of hidden neurons in each hidden layer, and $z_1$ illustrates the output parameter.

synthetic seismogram, we convolved the reflectivity series (derived from acoustic and density logs) with the wavelet derived from seismic data. The seismogram was then converted from depth to time domain using check-shot (borehole velocity survey) data from control wells. The synthetic seismogram was then correlated with seismic traces to create an impedance model in terms of a series of reflection coefficients. To generate the synthetic trace for this dataset, we used a Ricker wavelet with a dominant frequency of 30 Hz, a sample rate of 2 ms, and sample lengths of 128 ms. A plot of a synthetic seismogram and related reflectivity series, extracted wavelet, and well-to-seismic calibration is shown in Fig. 4.

### 3.4. Deep-learning neural network

DNN is a kind of neural network with several hidden layers trained using backpropagation-type algorithms. It consists of three types of layers; an input layer, hidden layers, and an output layer. All neurons in each layer are fully connected to the neurons of the next layer. The structure of the DNN model is shown in Fig. 5. It includes signal-forward and error back-propagation processing. We enter a sample data into the input layer during forward propagation, processes it as per the hidden layer's activation function, and continue to the output layer. The network's actual output is then compared to the expected output for that particular input. If the actual result is different than the expected result, the error back-propagation process is used to repeat this process (Dell'Aversana, 2019; Moosavi et al., 2019). During back-propagation, the weights and biases of each layer are continuously updated through various parameter optimization methods so that the actual output is closer to the expected results (Nguyen and Bui, 2019; Nguyen et al., 2020). The output of a neuron is shown in Eq. (13):

$$Y_j^k = f\left[\sum_{i=1}^{m} W_{ij}^h X_i^k + b_j^k\right] (j = 1,\ 2, \ldots) \tag{13}$$

where $Y_j^k$ is the output of the $j$ neuron in the layer $k$, $f$ for the activation function, $W_{ij}^h$ indicates the connection weights of the $i$th neuron in the layer k–1 and $j$ neuron in the layer $k$, $X_i^k$ represents the $i$ component of input sample data $X^k$, and $b_j^k$ is used for the bias of the $j$ neuron in layer $k$.

To calculate the error in back-propagation, the predicted and actual values of the neural network should be computed using Eq (14):

$$e_k = \frac{1}{2}\sum_{i=1}^{n}(d_i - Y_i) \tag{14}$$

where $d_i$ is the actual value, and $Y_i$ is the predicted value.

From Eqs. (13) and (14), the error function, $e_k$ can be calculated for each neuron. This process makes it possible to continually modify the neural network's weights and biases so that the predicted output is closer to the desired results. Taking $W_{ij}$ as the connection weight and $b_i$ as bias of the $i$th neuron in the hidden layer and the $j$ neuron in the output layer of the DNN, the updated mode of the value $l$ to the value $l+1$

can be found from Eqs. (15) and (16):

$$W_{ij}(l+1) = W_{ij}(l) - \eta\delta_i Y_i \tag{15}$$

$$b_i(l+1) = b_i(l) - \eta\delta_i \tag{16}$$

where $W_{ij}$ $(l)$ denotes the weight coefficient taken from the $l$ training step and $\eta$ is learning rate (often in the range of 0, 0.5), $\delta_i$ is the gradient of the performance function, $Y_i$ is a derivative of $Y_i$, and $b_j$ $(l)$ indicates the bias obtained from the $l$ training step.

In this study, the designed model consists of mainly two modules, (i) optimization of multiple seismic attributes and (ii) construction of the DNN. In this model, we used unsupervised learning to optimize seismic attributes that are sensitive to reservoir fractures. It was then fed into supervised learning to improve reservoir fracture prediction reliability and effectiveness.

#### 3.4.1. Optimization of seismic attributes

Optimization of seismic attributes is the basis for predicting reservoir properties such as porosity, saturation, and lithology. There are many different seismic attributes, and each makes a substantial contribution to seismic oil and gas reservoir prediction. In this particular study, we selected those seismic attributes sensitive and contribute more to reservoir fracture prediction through cluster analysis. Cluster analysis can highlight the specific features such as faults, fractures, and channels in seismic attributes, which are further combined with expert experience to improve the supervised learning process's efficiency. Cluster analysis combines seismic attributes based on the degree of information similarity. The information with a high degree of similarities was clustered, which continued until the seismic data was divided into several attribute aggregations based on detailed characteristics, completing the cluster analysis process. We customized multiple seismic attributes based on cluster analysis data, author domain knowledge, and proven reservoir characteristics, including (a) instantaneous phase, (b) instantaneous frequency, (c) RMS amplitude, (d) instantaneous amplitude, (e) average peak amplitude, and (f) arc length amplitude.

#### 3.4.2. DNN construction

According to the input data characteristics and output results, we decided the number of nodes in the input and output layers for DNN construction. However, the method of determining the number of nodes in the hidden layers is fairly complicated. We did this by training the neural network with various numbers of nodes in the same data set to find the number of hidden layer nodes that can limit the error to the smallest. Eq. (17) gives out the number of nodes in the hidden layer (Zhang and Ruan, 2009):

$$h = \sqrt{k+l} + a \tag{17}$$

where $k$ denotes the number of nodes in the input layer, $l$ stands for the number of nodes in the output layer, and $a$ is an uncertain value between 1 and 10, which can be set during the training process in specific conditions.

**Table 1**
Test errors of Sigmoid, Tanh, and Relu activation functions.

| Activation function | Error |
|---|---|
| Sigmoid | 0.4260 |
| Tanh | 0.0655 |
| Relu | 0.0114 |

#### 3.4.3. Activation functions

We used an activation function to ensure that each DNN layer's output is not a linear combination of inputs and to take advantage of their nonlinearity over the whole network. The activation functions Sigmoid, Tanh, and Relu are widely used (Fig. 6). We checked the errors in each of the three activation functions and found that the Relu activation function had a minimal error. (Table 1). We noticed that the activation function in the hidden layer had changed the output of certain neurons to zero during neural network training. This phenomenon not only reduces parameter interdependency (effectively addressing the overfitting problem in the training process), but it also improves neural network training performance. Since the Relu activation function can increase the network's nonlinearity, it was selected for this analysis (Fig. 6c).

#### 3.4.4. Hyperparameter selection

To obtain the best model, we designed the corresponding neural networks using the selected training datasets. DNN efficiency and capacity improve as the number of hidden layers increases. Too many hidden layers, on the other hand, can result in structural complexity, poor training performance, high generalization error, and high computational cost. We calculated the number of hidden layer nodes using empirical equations. To make predictions, a neural network model with varying numbers of hidden layer nodes was used. The neural network's mean square error (MSE) was accomplished with nine hidden layers (Fig. 7a and b). We noticed that when the neural network training epochs crossed 20000, the MSE was 0.001, fulfilling the accuracy criteria. We learned that as the number of hidden layers increases at the same training epoch, the MSE decreases and eventually becomes stable (Table 2). After 20000 training epochs, the MSE with seven hidden layers reaches the given threshold (i.e., $10^{-3}$), as shown in Fig. 7a and b. We proved that a network of seven hidden layers is adequate for predicting reservoir fractures and was chosen for this study.

### 3.5. DNN for lithofacies identification

In DNN seismic inversion, first, we set one-to-one samples using the seismic trace (attribute). Second, we used the logging curve to generate the sample sets for training, validation, and testing. A uniform sampling method based on well and lithofacies was used to solve missing

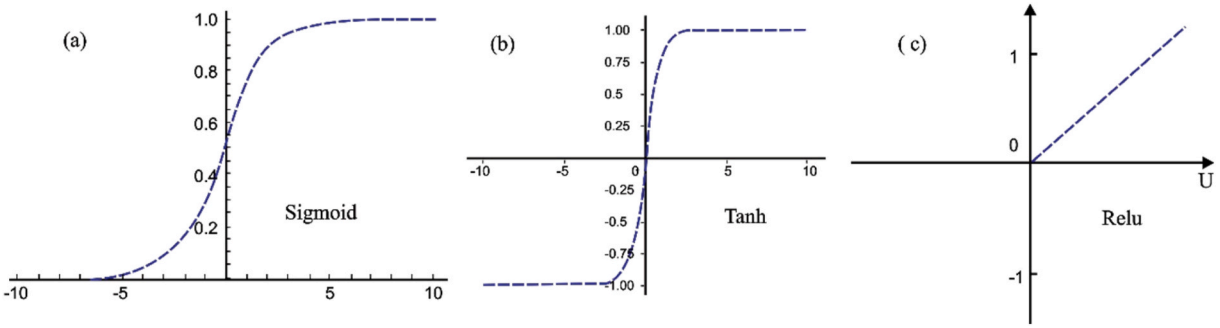


**Fig. 6.** Errors test in all three activation functions, (a) Sigmoid, (b) Tanh, (c) Relu.

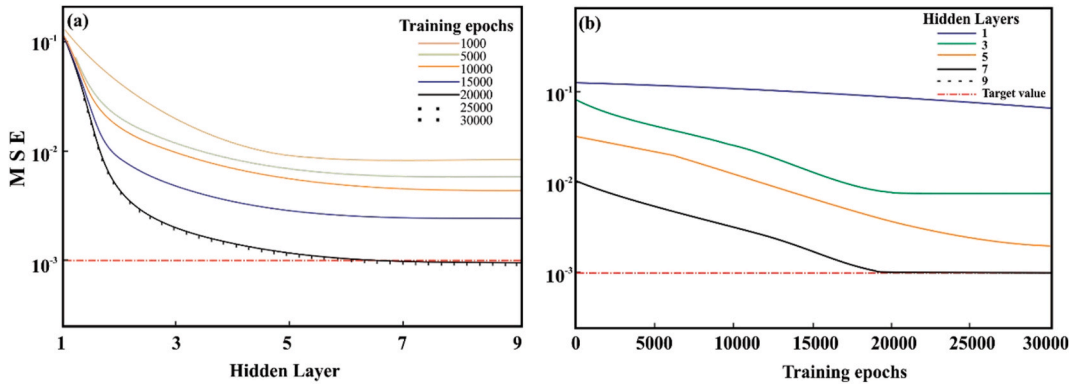


**Fig. 7.** DNN performance curve, (a) MSE versus hidden layer, (b) MSE versus training epochs.

**Table 2**
MSE for different hidden layer numbers in neural networks.

| Training Epochs | Hidden Layer One | Hidden Layer Three | Hidden Layer Five | Hidden Layer Seven | Hidden Layer Nine |
|---|---|---|---|---|---|
| 1000 | 0.111 | 0.052 | 0.016 | 0.015 | 0.015 |
| 5000 | 0.109 | 0.022 | 0.008 | 0.007 | 0.007 |
| 10000 | 0.107 | 0.012 | 0.007 | 0.006 | 0.005 |
| 15000 | 0.106 | 0.006 | 0.004 | 0.004 | 0.004 |
| 17500 | 0.105 | 0.005 | 0.003 | 0.003 | 0.003 |
| 20000 | 0.105 | 0.003 | 0.003 | 0.001 | 0.001 |
| 22500 | 0.104 | 0.003 | 0.002 | 0.001 | 0.001 |
| 25000 | 0.104 | 0.003 | 0.002 | 0.001 | 0.001 |
| 30000 | 0.104 | 0.003 | 0.002 | 0.001 | 0.001 |

lithofacies details to retain the network's predictive capabilities. Fig. 8 illustrates lithofacies grouping and uniform sampling for each well graphically. We divided the well's lithofacies curve into three types and extracted the M frequency division data from the sidetrack to build a vector ($X_1$, $X_2$, $X_3$, …, $X_M$). The number of sidetracks is listed in reverse chronological order (*1n*). We put the vector in the relevant lithofacies set based on the lithofacies group it belongs to, representing a sample set. Notice that lithofacies 1 has 4 samples at time intervals of 1, 2, 3, and 9, lithofacies 2 has 6 samples at time intervals of 4, 5, 6, 7, 14, and 15, and lithofacies 3 has 7 samples at time intervals of 10, 11, 12, 13, 16, 17, and 18, respectively (Fig. 8). We define three sets of data after lithofacies grouping and uniform sampling. Finally, we divide these three sets into classification and recognition sets with similar time intervals. The input was the frequency division attribute, and the learning target was the multi-well seismic lithofacies curve, e.g., the label. The first step began with the frequency division data, training the data from the bottom of the network before the network's top was achieved, an unsupervised training method. The second step began with the multi-well seismic lithofacies curve, transferred the error step by step from the top to the bottom of the network through back-propagation, and optimized the network layer by layer until it was developed. The validation process was adjusted based on the results obtained at each training epoch during the network's testing. Finally, we developed a sophisticated functional network that can predict and transform seismic lithofacies based on the frequency division attribute.

## 4. Results and discussion

### 4.1. Reservoir characterization

Thin sections were used to examine the fractures and connected and non-connected pores (Fig. 9a–f). We know that the most common reservoir pores are fractures, dissolution pores, and intergranular pores. Thin sections indicate a micritic matrix crossed by fractures of varying sizes in different directions. The majority of the fractures are open-mode with a wide fracture aperture, while others are filled with epigranualar sparitic cement (Fig. 9a–d, and f). It is worth noting that tiny dissolved pores developed alongside those fractures served as another primary

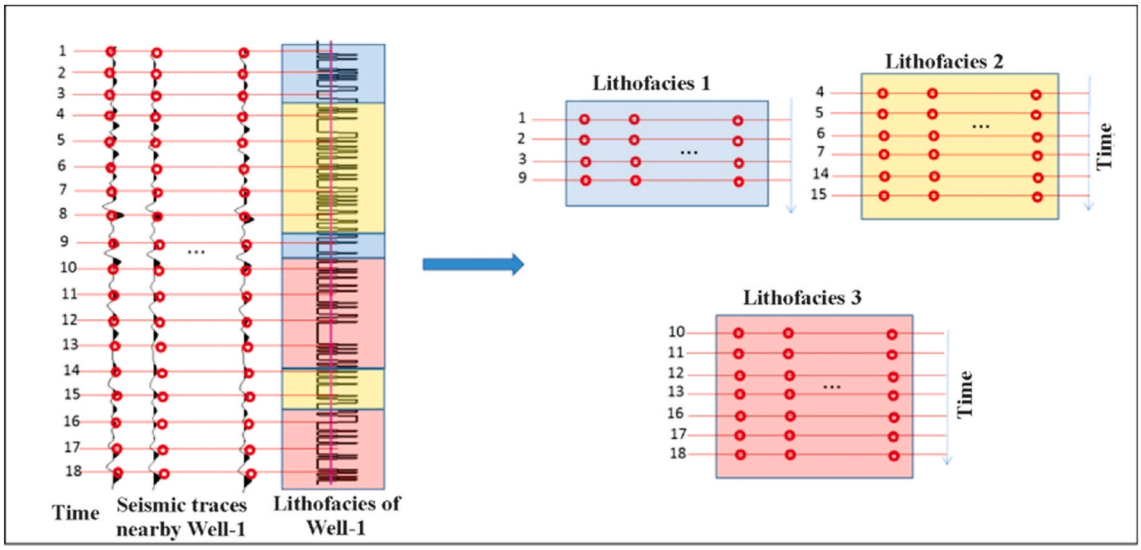


**Fig. 8.** The architecture of the uniform lithofacies assemblages.

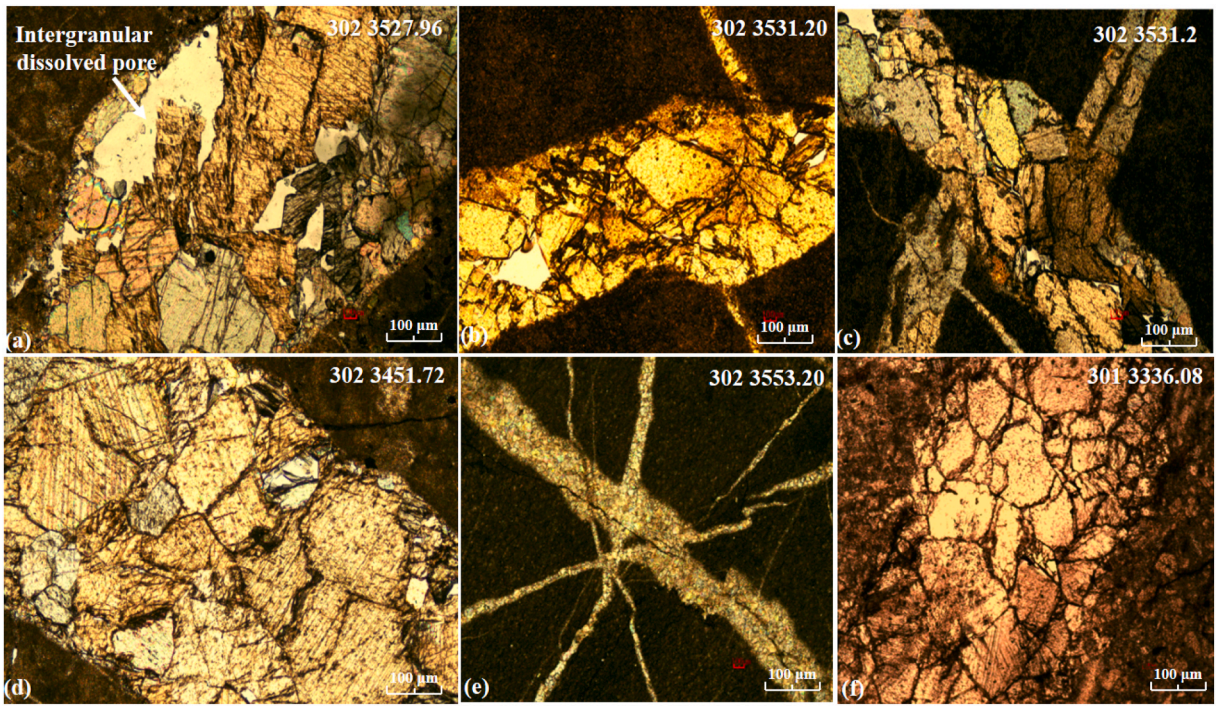


**Fig. 9.** Thin sections of Paleozoic reservoir in the oilfield X, (a) network fracture in calcite; (b) open fracture in dolomite at 3531 m; (c) open fracture in dolomite at 3531.2 m; (d) fracture zone in dolomite at 3451 m; (e) open fractures and pores at 3553.2 m; (f) micro-fractures developed in dolomite.

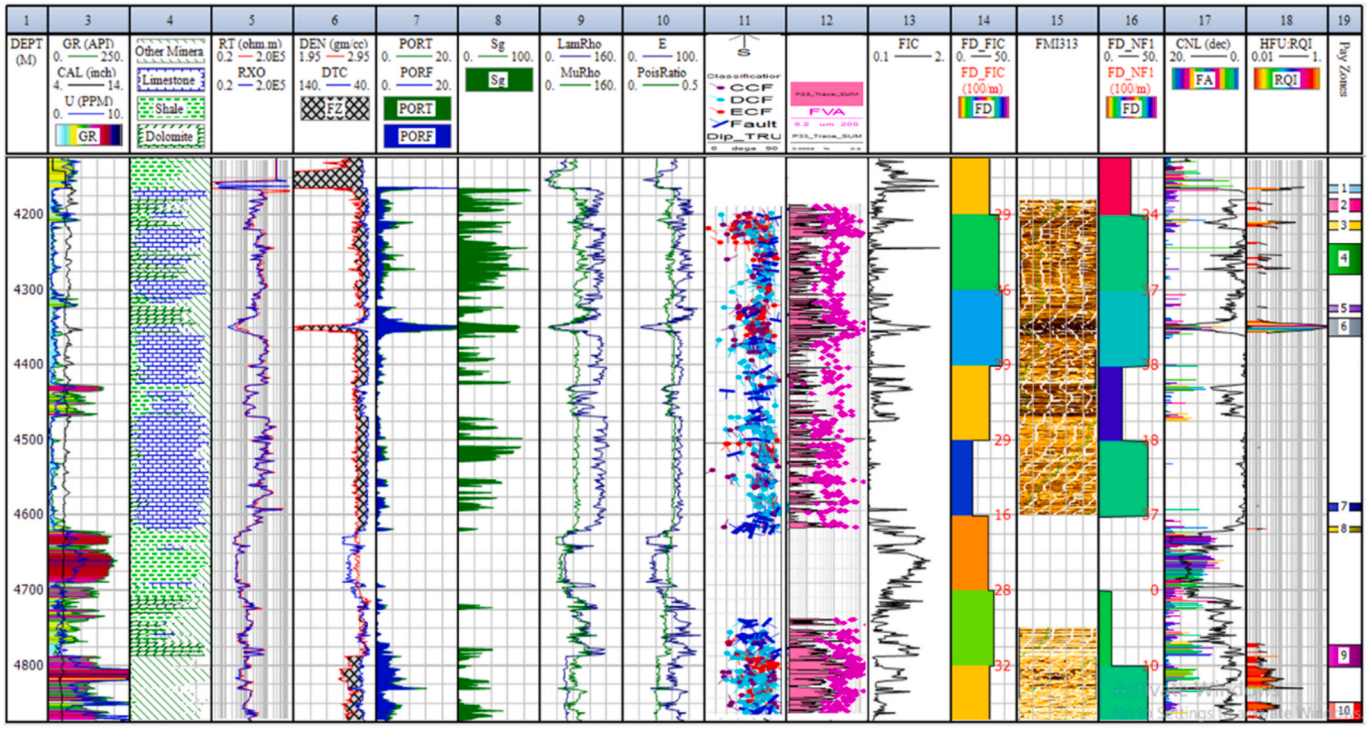


**Fig. 10.** Computed results of petrophysical parameters and characterization of fracture parameters for 313 well. FVA is fracture aperture from the FMI log, FA is fracture aperture calculated from the FIC model, FD is fracture density from the FIC model, and RQI is reservoir quality index.

reservoir storage space in the study area. The thin sections show calcite, dolomite, and biotite dissolution, as well as several micro-pores with a diameter of around 1 μm. In Fig. 9a, we see some hydrocarbon along the intergranular dissolved pore. Fig. 9e depicts a fracture-filled with calcite as a result of late diagenesis. Other fractures cross the fractures, and styloliths impact their cement in various directions (Fig. 9b, c, e). This complex heterogeneity and the intersection of the fracture networks lead to an increase in porosity by enhancing the interconnection between the existing pores.

### 4.2. Estimating fracture parameters from the FIC model

#### 4.2.1. Comprehensive evaluation in well 313

The comprehensive evaluation of the fractured carbonate reservoir in the 313 well is shown in Fig. 10. The FIC logging curve (track 13) exhibits abnormal behavior or deflection along fractured zones (track 11), indicating cracks or natural fractures in the reservoir interval. Notably, the curves of fracture porosity (PORF) and hydrocarbon saturation ($S_g$) (tracks 7 and 8) as well as elastic parameters (tracks 9 and 10) indicate deflection or non-steady behavior across the deflection of the FIC model curve. A good correlation between high fracture and total porosity regions with the FIC model curve deflection will help researchers and explorers to identify favorable fracturing sweet spot. It also adds credibility to the workflow used in the research. When the FIC model curve is compared to the measured fracture zones and fracture aperture from the FMI log (tracks 11 and 12), the results are remarkably consistent and uniform.

It should be noted that uranium has a more positive impact on the FIC model (track 1). Consequently, using the GR log, the FIC model produces improved results for detecting natural fractures in the reservoir. It is important to note that the length of the deflected curve (track 17) indicates the size of the fracture aperture, which is validated by high values of neutron porosity log (CNL) and measured fracture aperture from FMI logging data (track 12). The predicted (track 17) and measured (track 12) fracture apertures are consistent throughout the interval. These findings strengthen our confidence in the prediction model's accuracy. According to (Aghli et al., 2019), porosity logs such as NPHI and PHIE show high-porosity spikes along fracture zones, particularly when the fractures are open. As a result, porosity logs are the best logging tool for determining fracture aperture. The number of fractures in specific zones can be measured by counting the number of deflected curves per 100 m (track 14). Furthermore, we validate the predicted fracture density by counting the number of faults/fractures in FMI log data (track 16).

Some areas in the reservoir interval where shale is the dominant lithology, and no FMI log was recorded, but the FIC model picked up or identified the fracture signature in those areas (e.g., 4600–4700 m). It should be noted that peaks or deflections in the gamma-ray log across natural fractures can often reflect conductive fractures in which soluble compounds or radioactive materials invade the fracture.

According to the interpretation of the 313 well, depths ranging from 4320 to 4325 m and 4340–4355 m have high fracture intensity and good fracture aperture, which is supported by high CNL and fracture porosity values. Furthermore, the reservoir quality index (RQI) indicates good values in certain fracture zones, i.e., RQI $>$ 0.4. Also, we see that the density curve has low values along high RQI, indicating a gas anomaly. The high gas saturation (Sg) values in Fig. 10 (track 7) confirm this. Appendix A contains more detail on calculating elastic and petrophysical parameters, such as RQI and mineralogical composition.

Fig. 12 shows a further enlarged (zoomed-in) portion of Fig. 11 that indicates the range of fracture porosity and identified fractures in the productive zone (4342–4354 m) of the 313 well. Note that the dominant lithology in this zone is limestone and dolomite.

#### 4.2.2. Comprehensive evaluation of well 306

Fig. 13 shows a comprehensive evaluation of the 306 wells. In this well, the FIC model curve exhibits deflection across the fracture porosity (track 5) and permeability (track 7) curves, as well as the fracture index (FI) and elastic parameters (tracks 8, 9, and 11). The FIC model deflection along with low density and high sonic travel time (AC) values show possible gas zones (track 6). Furthermore, the presence of high total and fracture porosities and permeability results in a more positive deflection of the FIC model curve (track 5 and 7). Comparing predicted and measured faults/fractures density in particular zones shows good agreement (track 13 and 15). The length of the deflected curve (fracture aperture) is large, along with the high porosity, permeability, and RQI (tracks 16 and 17), as evidenced by higher neutron porosity log values (CNL). Limestone and dolomite are the dominant lithologies along the

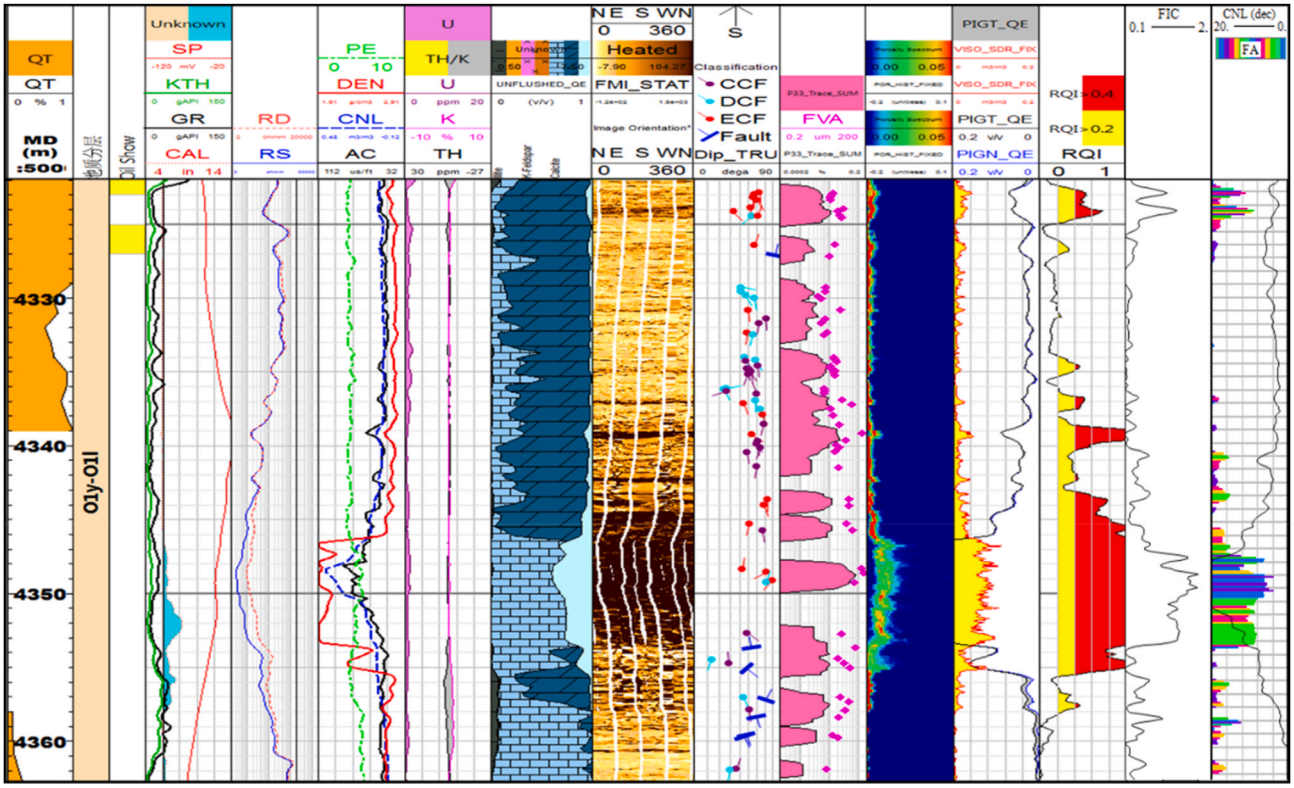


**Fig. 11.** Zoom in on calculation results of fracture parameters of the 313 well (a portion of Fig. 13 from 4320 to 4362 m).

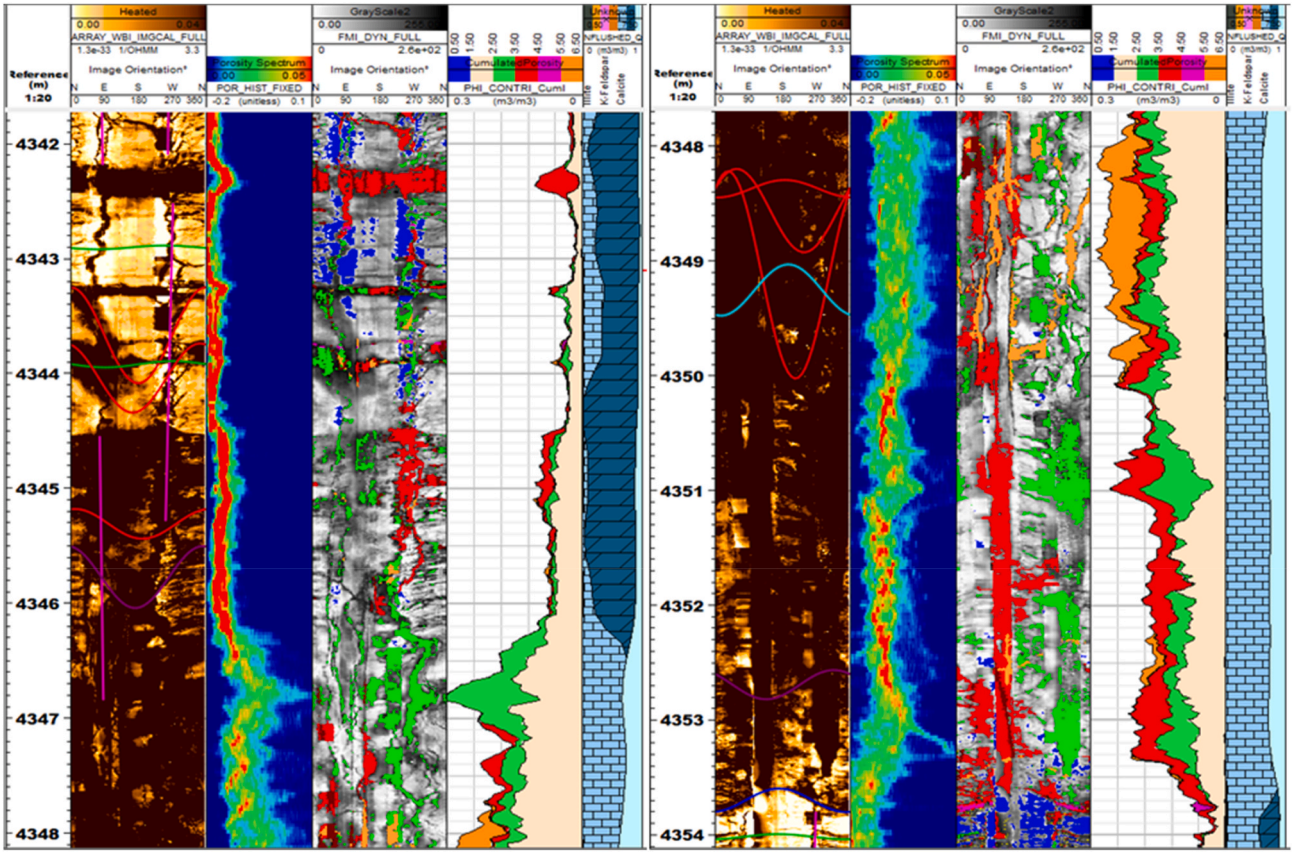


**Fig. 12.** The range of fracture porosity and identified fractures in the productive zone of 313 well (zoom in on a portion of Fig. 11 from 4342 to 4354 m).

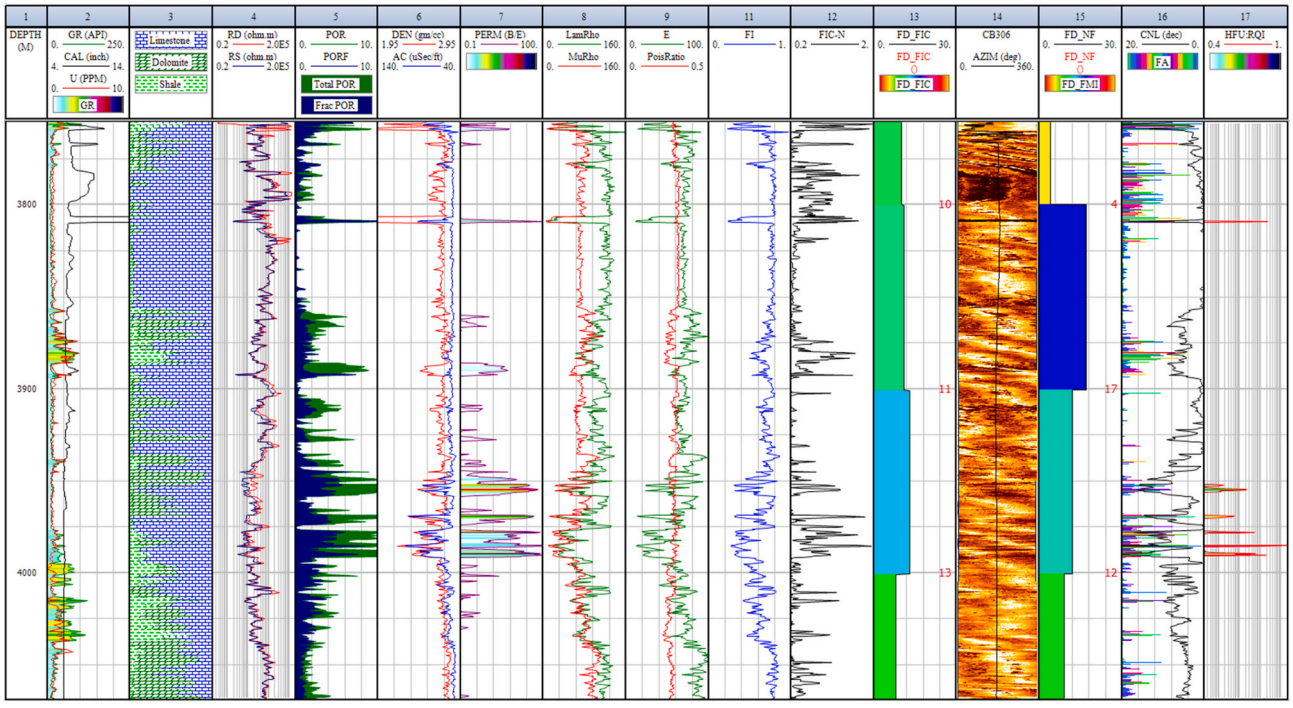


**Fig. 13.** Calculation results of petrophysical parameters and characterization of fracture parameters for 306.

high-density FIC model curve (track 3).

A comprehensive evaluation of the key wells confirmed the validity of the proposed FIC model for fractures evaluation as highly correlated with the FMI logs and core data. Also, the proposed FIC model proved to be very effective in measuring fracture aperture in intervals where acoustic and electrical imaging tools could not detect this parameter.

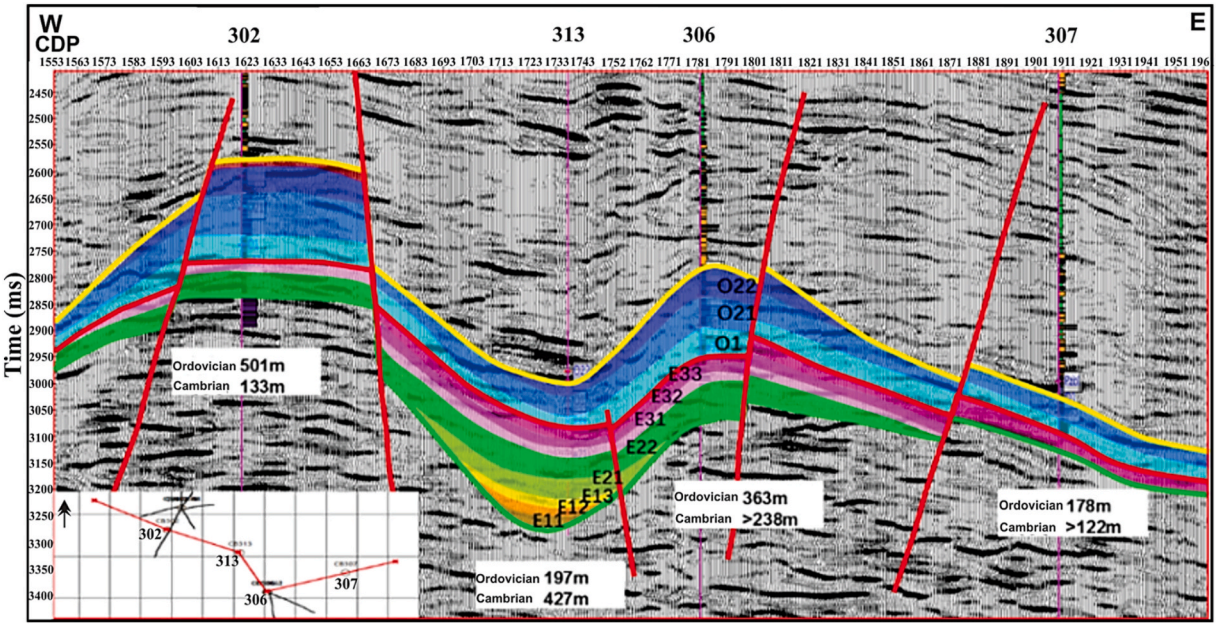


**Fig. 14.** Interpreted seismic section of Paleozoic reservoir along the east-west.

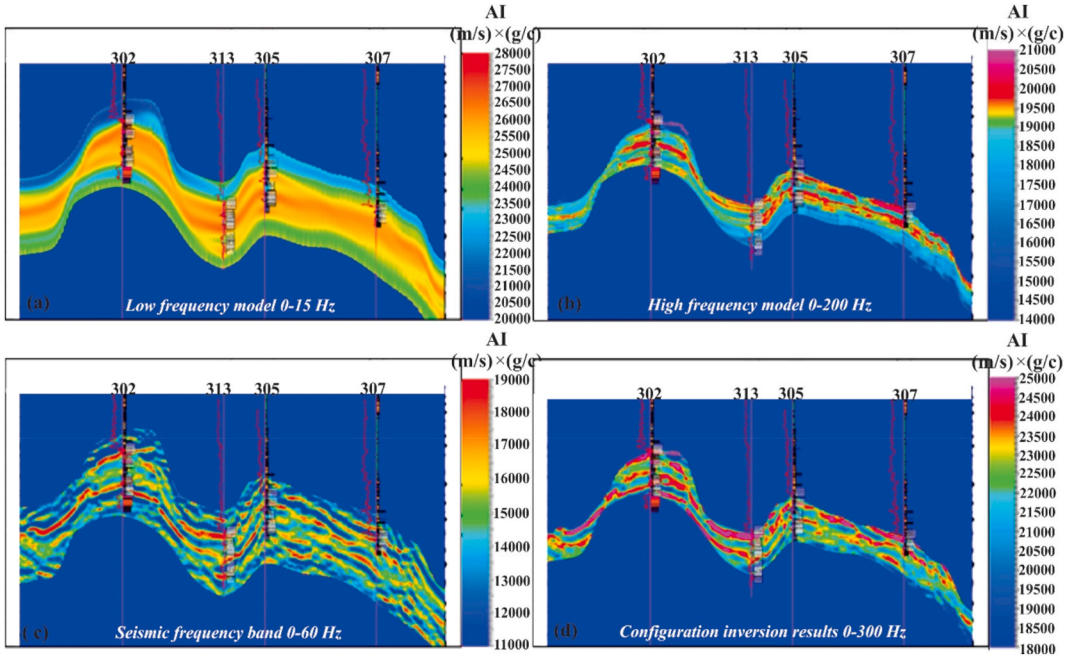


**Fig. 15.** The inverted AI profile, (a) low-frequency model 0–15 Hz, (b) high-frequency model 0–200 Hz, (c) frequency band between 0 and 60 Hz, (d) final inversion model 0–300 Hz.

Therefore, fracture aperture is considered the critical parameter for determining fractures' effect on the porosity and permeability system.

### 4.3. Reservoir evaluation from seismic inversion using DNN inversion strategy

#### 4.3.1. Seismic data interpretation

Before we can perform seismic inversion, we must first interpret the seismic data. The interpretation profile of the top and bottom structure of Paleozoic horizons is shown in Fig. 14. According to the interpreted results, the target reservoir (Paleozoic strata) gradually thins from west to east. Furthermore, we can see the structural High in the west and structural Low in the east. The entire study area is covered by a combination of normal and thrust sheets locally cut by strike-slip faults.

#### 4.3.2. Acoustic impedance inversion

The seismic data in this field is poor in low-frequency components below 10 Hz and high-frequency components above 60 Hz. As a result, frequency division modeling and random simulation inversion with low- and high-frequency components are needed (Luo et al., 2016). The results of different frequency component models and final configuration inversion applied to the interpreted 3D seismic volume are shown in Fig. 15. The effects of random simulation inversion based on 0–15 Hz frequency interpolation, 0–200 Hz under the constraint of the seismic

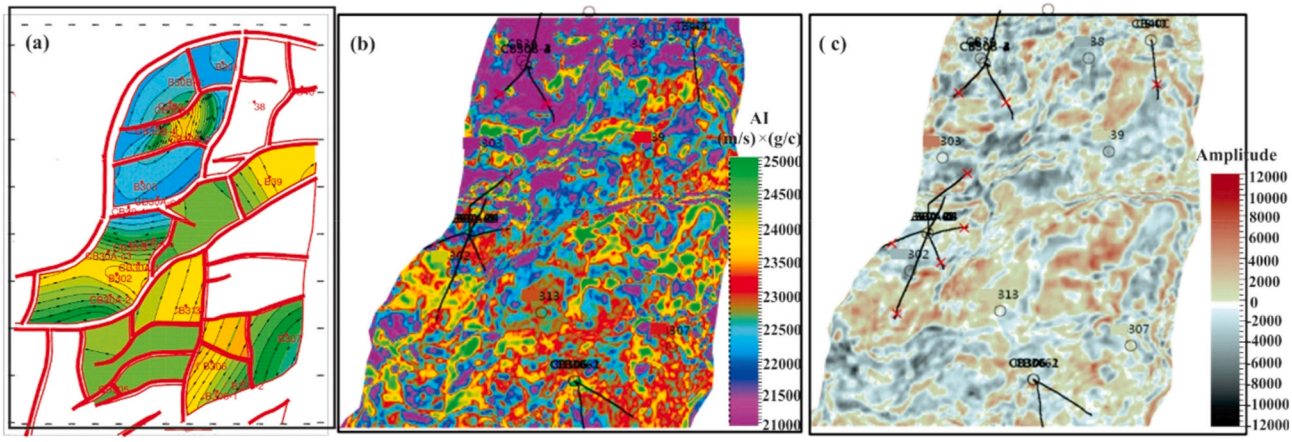


**Fig. 16.** (a) Seismic structural map, (b) inverted AI slice, (c) amplitude slice. The lateral variations of AI and amplitude are well-correlated.

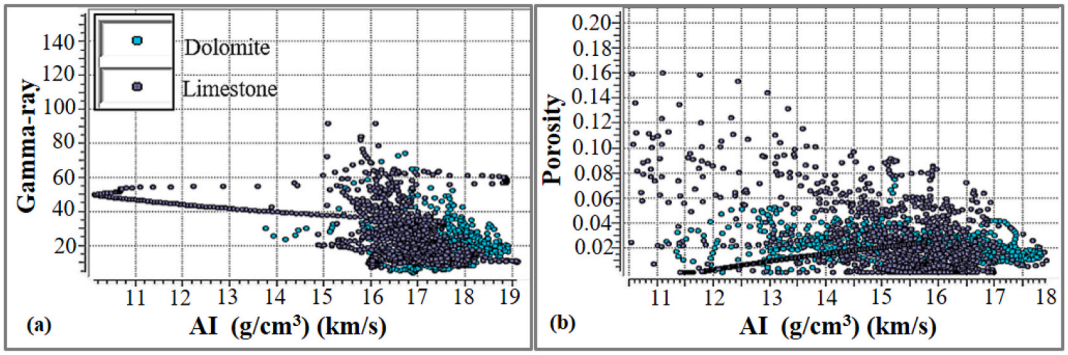


**Fig. 17.** Correlation of rock physics and petrophysical parameters, (a) GR versus AI, (b) porosity versus AI.

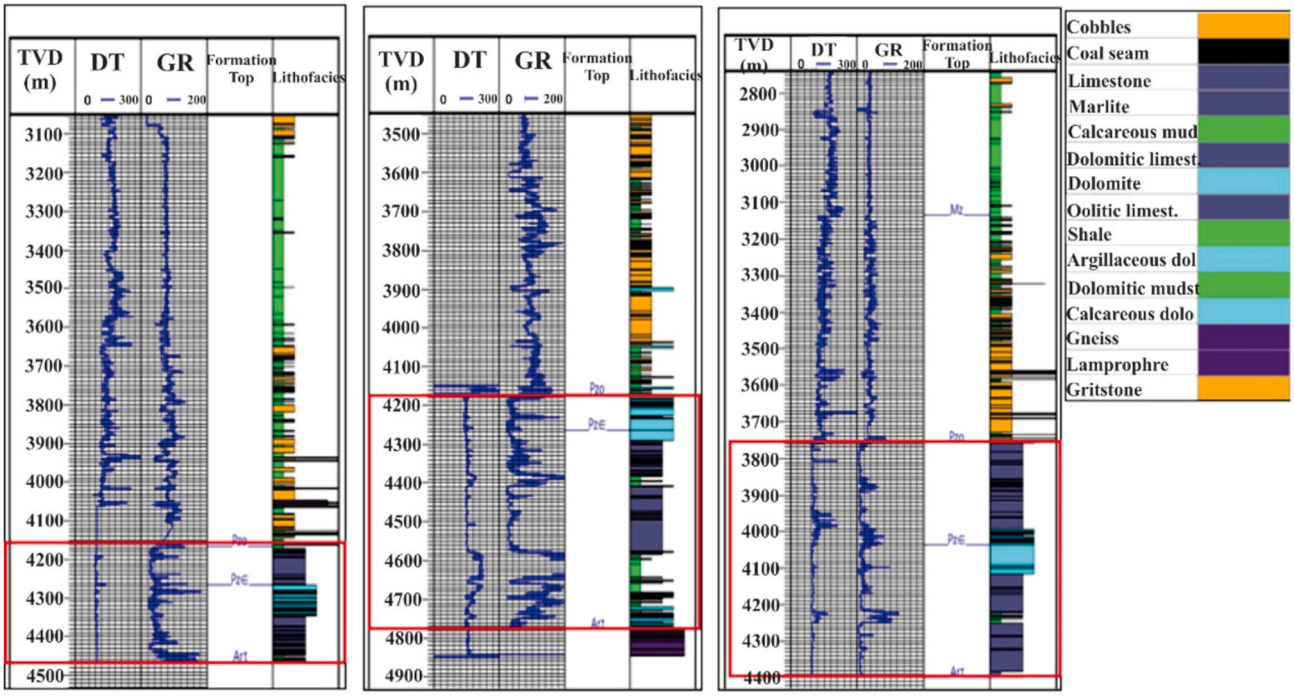


**Fig. 18.** Lithological interpretation of Paleozoic strata in key wells.

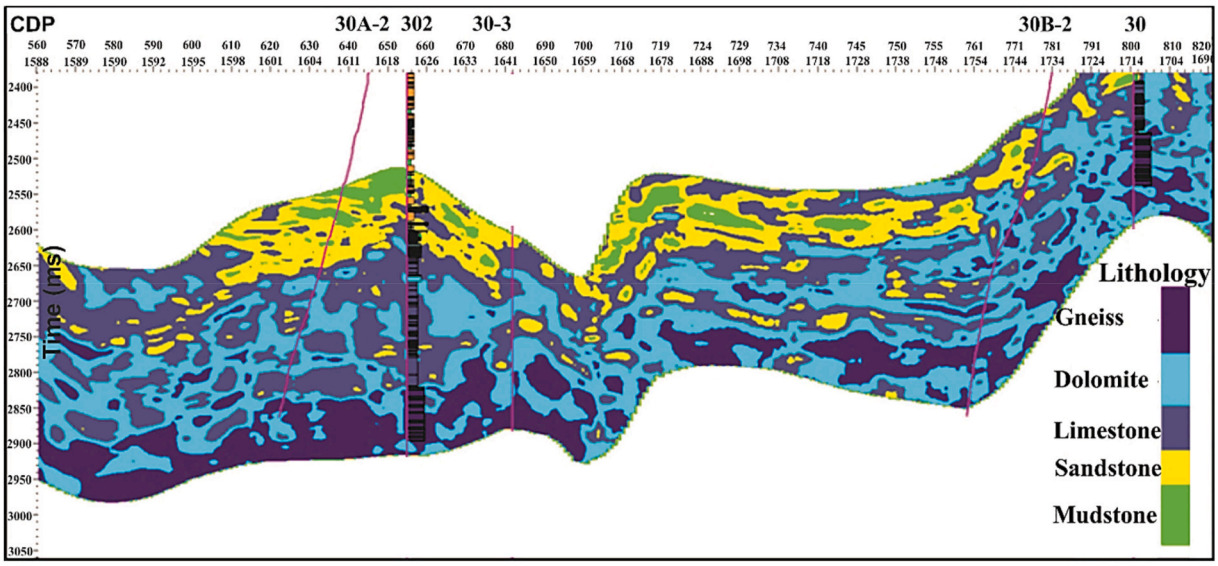


**Fig. 19.** Seismic lithofacies inversion profile using DNN inversion strategy.

waveform, and a frequency bandwidth of 0–60 Hz are shown in Fig. 15 (a–c). The inversion result demonstrates a certain similarity between seismic reflection characteristics and vertical wells. The final configuration inversion result using the well profile is shown in Fig. 15d. We observe that the high part of the buried hill has a relatively high impedance (unconformity surface and downward). The proposed DNN inversion strategy captured vertical and lateral variations in AI with high resolution while retaining structural reflection characteristics in the seismic frequency band. The inverted impedance surface from the DNN inversion strategy matches the impedance log well. As a result, the 0–300 Hz impedance inversion tests are valid and can be used to quantify seismic lithofacies and reservoir parameters.

Fig. 16(a–c) shows the seismic structural map, amplitude slice, and AI inversion under the lower Paleozoic top surface in the buried-hill. Comparing amplitude slice with configuration AI inversion slice indicates high seismic lateral resolution (Fig. 16b and c). The reflection morphology (amplitude) is well-correlated with the lateral variations of AI and geological structure. The area around wells 30, 302, 313, and 306 is characterized by a high amplitude seismic response and high AI, indicating fracture zones.

### 4.3.3. *Seismic lithofacies calculation*

Rock-physics analysis plays a key role in bridging the gap between rock parameters and seismic data to improve the prediction accuracy of complex sedimentary structures (Al Moqbel and Wang, 2011; Ashraf et al., 2019). A cross-plotting between GR versus AI and porosity versus AI is generated to establish the relationship between AI, GR, and porosity (Fig. 17a and b). The nonlinear relationship between AI, GR, and porosity (i.e., high AI $>$ 15000 (m/s) (g/cm$^3$) and low GR) refers to limestone and dolomite lithofacies with moderate to low porosity.

We use the GR and DTP logs to classify the lithofacies in 302, 30–3, and 30 wells. Fig. 18 demonstrates the lithological analysis of the buried-hill Paleozoic strata (shown with red box). We observe that the buried-hill comprises mainly of dolomite and limestones (GR $<$ 20) with a minor fraction of shale and sandstone (GR $>$ 70).

The lower Palaeozoic seismic lithofacies profile characterized five different types of lithofacies distribution (Fig. 19). The limestone and dolomite distribution dominates the seismic lithofacies profile around wells 30 and 30B-2, while limestone and sandstone are dominant in wells 302, 30A-2, and 30–3. It is worth noting that the results of the lithofacies inversion meet with the logging interpretation and geological settings (Fig. 18).

Note that the AI varies from 11000 to 25000 (g/c) (m/s) in the study zone (lower Paleozoic), which corresponds to dolomite and limestone lithofacies with subordinate shale and sandstone lithofacies around well 302 (Fig. 15). The variations in AI are closely related to facies-related changes, i.e., the high AI region (18000–25000 (m/s) (g/c) corresponding to dolomite and limestone beds. A probabilistic study of lithofacies revealed a strong correlation between limestone and dolomite lithofacies with a high AI (Liu et al., 2016; Yasin et al., 2020a). It is shown that the DNN inversion strategy can construct and constrain the spatial distribution of facies and reservoir parameters as a result of this good calibration.

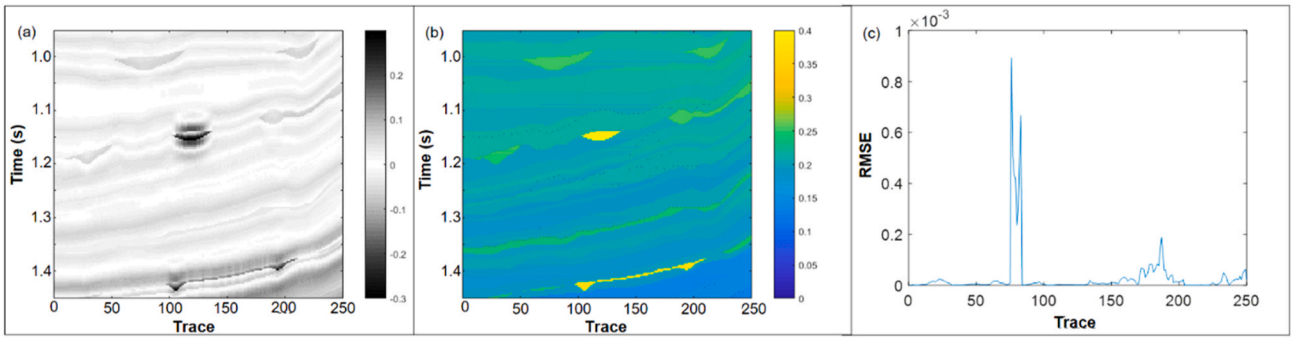


**Fig. 20.** The synthetic and porosity models, (a) synthetic seismic, (b) inverted porosity model, (c) the RMSE.

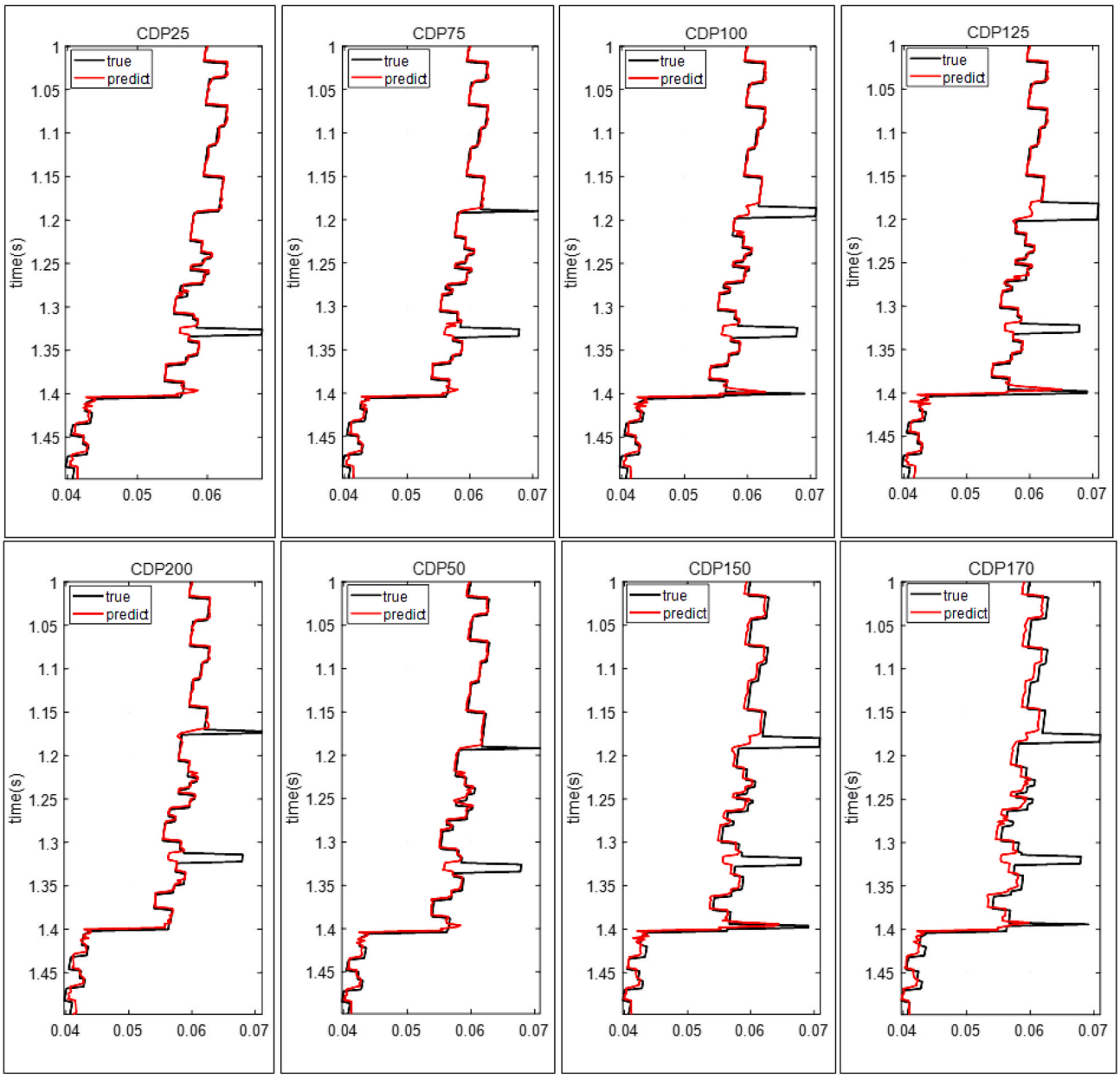


**Fig. 21.** Comparison of the estimated and actual porosity curves (red line represents the predicted results and the black line represents true values). (For interpretation of the references to color in this figure legend, the reader is referred to the Web version of this article.)

### *4.4. Porosity and FIC model prediction from seismic inversion*

#### *4.4.1. Numerical simulation (porosity)*

We designed a complex Marmousi II model (Martin et al., 2006) to check further the DNN inversion strategy's ability to predict porosity. The model´s input synthetic seismic response, inverted porosity, and root mean square error (RMSE) of each trace are shown in Fig. 20.

We used several traces (CDP25, CDP50, CDP75, CDP100, CDP125, CDP150, CDP170, and CDP200) as pseudo wells to develop a numerical model. The porosity of all eight pseudo wells was assumed to be known for seismic records of the model during the testing period. To establish the mapping relationship between seismic data and logging porosity, we trained the DNN model. We used CDP25, CDP75, CDP100, CDP125, and CDP200 as learning samples and CDP50, CDP150, and CDP170 as testing samples to train the model. The predicted and real porosities at various CDPs are compared in Fig. 21. Because of the nonlinear relationship between the inputs and outputs, it is shown that outliers are not well captured. Indeed, true measurements are dependent on local variations in the physical properties of the subsurface in one or more neighboring points, which may be affected by a variety of environmental and measurement factors that cause some outliers to output data. As a result, instead of outliers, the DNN application is intended to have a stable amount of data. Finally, the trained model was used to estimate the spatial distribution of porosity using the seismic volume as input. The root mean square error (RMSE) of each trace is also less than 0.001, demonstrating the DNN inversion strategy's consistency and validity (Fig. 20b and c).

#### *4.4.2. Porosity and FIC model inversion*

We analyze the fracture porosity (PORF) calculation of deep-buried carbonate reservoirs using the relationship between AI and porosity (Fig. 22). According to the figure, the buried-hill's structural High and Low (unconformity surface and downward) have good fracture porosity and correlate well with logging porosity (PORF). As a result, the

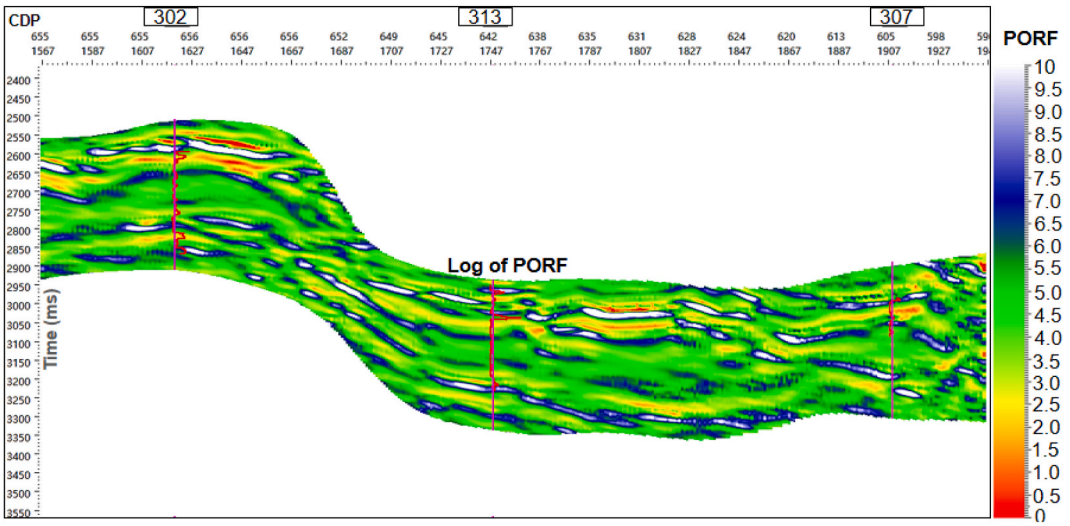


**Fig. 22.** The inverted porosity profile using DNN inversion strategy.

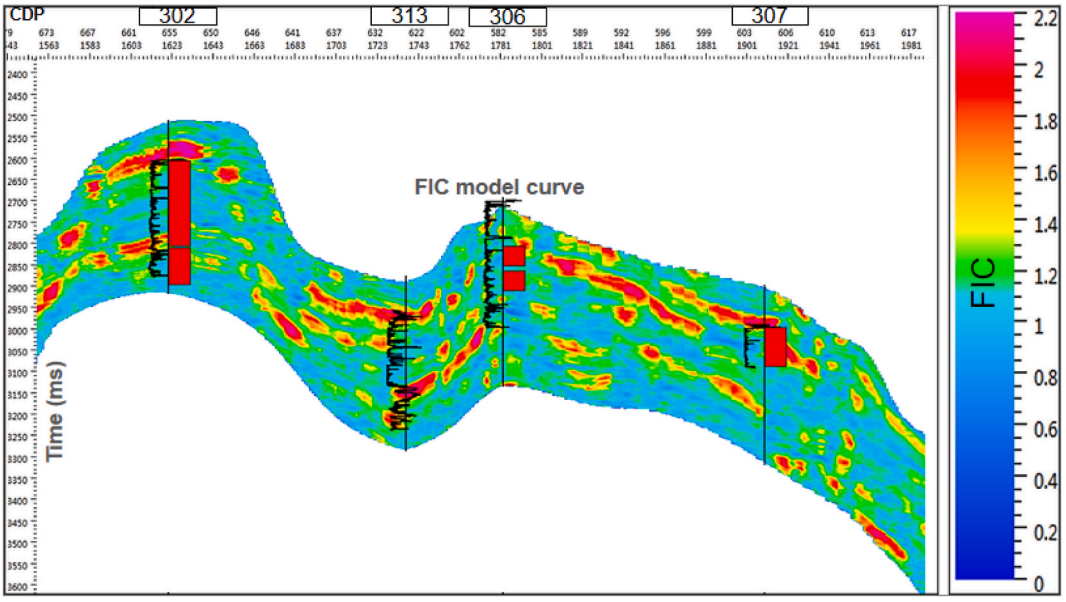


**Fig. 23.** The inverted profile of the proposed FIC model. The color bar shows the FIC model values. (For interpretation of the references to color in this figure legend, the reader is referred to the Web version of this article.)

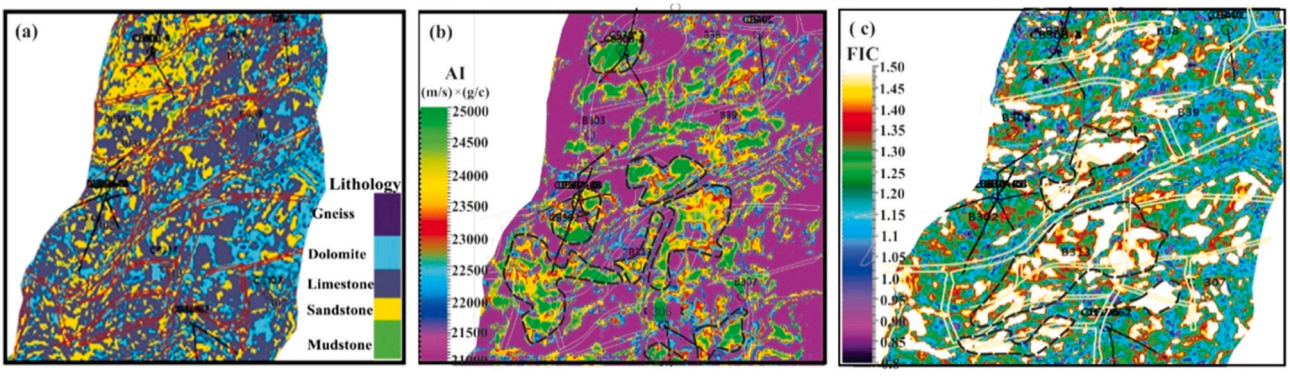


**Fig. 24.** The horizontal distribution inversion results, (a) lithofacies, (b) AI, (c) FIC model.

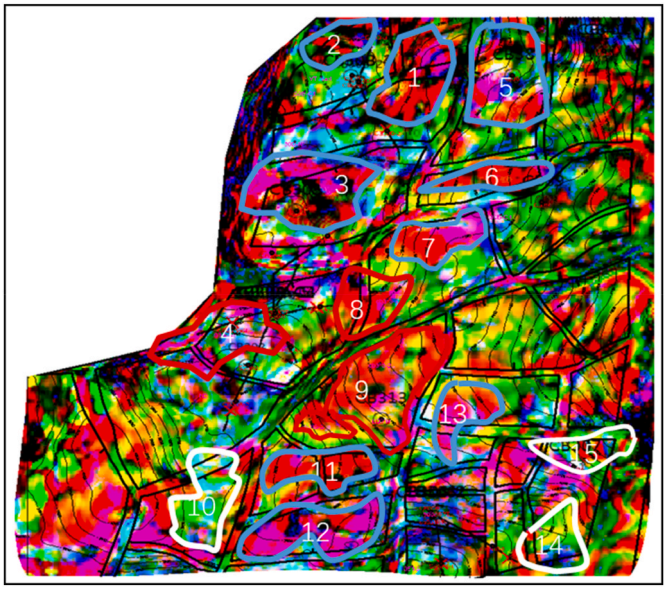


**Fig. 25.** RGB color blending map of fracture development areas for the lower Paleozoic buried-hill structure. (For interpretation of the references to color in this figure legend, the reader is referred to the Web version of this article.)

**Table 3**
Favorable areas for reservoir development.

| No. | Fault | Fracture development | Reservoir thickness (m) | Favorable area type |
|---|---|---|---|---|
| 1 | developed | I | <60 | II |
| 2 | developed | I | <60 | II |
| 3 | developed | I | <60 | II |
| 4 | developed | I | 100–160 | I |
| 5 | developed | I | <60 | II |
| 6 | Less developed | I | 60–100 | II |
| 7 | Less developed | I | 60–100 | II |
| 8 | developed | I | 120–160 | I |
| 9 | developed | I | 100–140 | I |
| 10 | developed | II | 40–80 | III |
| 11 | developed | I | 60–100 | II |
| 12 | developed | I | 60–100 | II |
| 13 | developed | I | 80–100 | II |
| 14 | Less developed | II | <60 | III |
| 15 | Less developed | II | <60 | III |

proposed DNN inversion strategy captured vertical and lateral variations in porosity with high resolution and a more tangible geological perspective. The results of the synthetic model and the DNN inversion strategy revealed an excellent vertical and lateral distribution of porosity. Additionally, the results demonstrate that the proposed inversion strategy is versatile and applicable to complex geological structure.

Fig. 23 demonstrates the spatial variation of reservoir fracturing parameters (e.g., the FIC model) in the inter-well regions. The inverted FIC model, based on its linear relationship with fracture porosity, highlights good fracture zones in the vicinity of wells 302, 313, 306, and 307, as well as high AI values (Fig. 15d). Dolomite and limestone are the dominant lithologies in these zones (Fig. 19). A good distribution of fracture parameters (high FIC model values corresponded to large fracture apertures) around wells 302, 313, 306, and 307, indicating potential reservoir zones. The horizontal distribution of the FIC model matches well with the inverted fracture porosity (Figs. 22 and 23).

### 4.5. Quantitative seismic prediction of sweet spots

To further investigate the plane distribution of fractures, we compare the planar distribution results of the FIC model with AI and lithofacies planer slices (Fig. 24a–c). We notice that the buried-hill fractures around wells 313, 306, and 307 are well-developed. Furthermore, the fractures southwest of well 302 and east of well 303 are well-developed (Fig. 24c). It should be noted that high fracture regions (Fig. 24c) have high AI values (Fig. 24b), dolomite and limestone are the dominant lithologies (Fig. 24a) (shown with black circles).

The quantitative seismic-predicted multi-attribute RGB (Red, Green, Blue) color blending technologies employing amplitude (green), AI (blue), and FIC model (red) show a well-developed fracture network along the major fault zones of wells 302, 306, and 307 (Fig. 25). The highlighted red and magenta zones are assumed to be faults and fractures. It is worth noting that the zones surrounding wells 305 and 303 have suitable reservoir thickness but a less well-developed fracture network, as interpreted by the attributes map produced by RGB color blending. The comprehensive evaluation of fracture development zones in the lower Paleozoic buried-hill reservoir is shown in Fig. 25 and Table 3. The figure represents well-developed fracture areas (marked with red circles) that are defined as class I reservoirs, while less-developed fracture areas (marked with blue and white circles) are defined as class II and class III reservoirs, respectively (Table 3).

## 5. Conclusions

In this study, we applied a comprehensive set of technical tools and research components to the seismic data in order to predict the high-quality reservoir regions of a complex buried-hill structure. After all, the following conclusions could be drawn:

1. The application of the proposed FIC model enabled us to successfully predict the fracture zones and fracture density in the buried-hill structure using a combination of conventional logs. Also, the FIC model proves effective in identifying the fracture aperture in zones where FMI data are lacking.
2. The log interpretation results for wells 313, 306, 307, 39, and 30 show high fracture intensity and good fracture aperture, confirmed by high neutron and fracture porosity. Also, RQI reflects good quality reservoir sections along the fractured zones (i.e., RQI $>$ 0.4). The bulk density curve shows low values against the fractured interval, which indicates a gas anomaly.
3. The proposed DNN inversion strategy trained by multiple seismic attributes is highly correlated to the logging interpretation and can provide more accurate results. Five different types of lithofacies distribution in the buried-hill structure are identified, where limestone and dolomite are dominant, with a minor quantity of shale and sandstone. The limestone and dolomite reservoir is mainly developed around 302, 306, and 307 wells, whereas the sandstone reservoir is dominant around 30 well. The results were consistent with the logging interpretation and geological settings.
4. The horizontal distribution of the FIC model matches well with the inverted fracture porosity profile. The planer slices of the high FIC model around wells 302, 313, 306, and 307 have high AI values, with dolomite and limestone are the dominant lithologies.
5. Based on a comprehensive analysis of the research results, the study area is divided into class-I, class-II, and class-III reservoirs according to well-developed, developed, and less-developed faults and fracture networks.

## Author statement

Qamar Yasin: Conceptualization, Methodology, Writing – original draft. Yan Ding: Geophysical Data Interpretation. Syrine B: Geological Data Interpretation. Qizhen Du: Supervision. Cyril D. Boateng:

Reviewing and Editing the Writing – original draft. Naser Golsanami: Petrophysical Evaluation.

## Declaration of competing interest

The authors declare that they have no known competing financial interests or personal relationships that could have appeared to influence the work reported in this paper.

## Acknowledgment

The National Science Foundation of China supports this research (41930429 and 41774139), the China National' 111′ Foreign Experts Introduction Plan for the Deep-Ultradeep Oil & Gas Geophysical Exploration. We are grateful to Beijing Rock Star Petroleum Technology Co., Ltd. for providing software support and lab facilities.

## List of abbreviations

| | |
|---|---|
| DNN | deep-learning neural network |
| FMI | formation micro-image |
| BP | backpropagation |
| K | permeability (mD) |
| ϕ | porosity (%) |
| $V_{sh}$ | volume of shale (vol) |
| $E_d$ | dynamic Young's modulus (GPa) |
| $\upsilon_d$ | dynamic Poisson's ratio |
| GR | gamma-ray |
| SP | spontaneous potential |
| LLD | deep resistivity |
| DTP | P-wave sonic (μs) |
| DTS | S-wave sonic (μs) |
| RHOB | density (g/cm$^3$) |
| NPHI | neutron porosity |
| FZI | flow zone indicator |
| RQI | reservoir quaity index |
| HFU | hydraulic flow unit |
| $V_S$ | shear wave velocity (m/s) |
| $V_P$ | compressional wave velocity (m/s) |
| FIC | fracture identification constant |
| FI | fracture index |
| AI | acoustic impedance (m/s) × (g/cm$^3$) |

## Appendix A

### *A1. Estimating the rock's parameters*

#### *A1.1 Multi-mineral modeling*

The multi-mineral modeling approach utilizes the relationship between log measurements and various minerals using a set of linear equations (Eq. (A1)). An additional unity equation with the sum of the individual mineral components and fluid proportions is 1 was included. The proposed model uses six equations to solve six unknowns: five minerals and porosity.

The log measurements used for the model are density ($\rho$), $V_P$, $Vs$, acoustic impedance ($AI$), and the parameter '$L$' equaling the product of density and photoelectric index, i.e., ($L = Pe \times \rho$), which can be written as in Eq. (A2)

$$\begin{aligned}
\rho &= \rho_{fl}{}^{*}\varphi + \rho_1{}^{*}M_1 + \rho_2{}^{*}M_2 + \rho_3{}^{*}M_3 + \rho_4{}^{*}M_4 + \rho_5{}^{*}M_5 \\
AI &= AI_{fl}{}^{*}\varphi + AI_1{}^{*}M_1 + AI_2{}^{*}M_2 + AI_3{}^{*}M_3 + AI_4{}^{*}M_4 + AI_5{}^{*}M_5 \\
V_p &= V_{pfl}{}^{*}\varphi + V_{p1}{}^{*}M_1 + V_{p2}{}^{*}M_2 + V_{p3}{}^{*}M_3 + V_{p4}{}^{*}M_4 + V_{p5}{}^{*}M_5 \\
V_s &= V_{sfl}{}^{*}\varphi + V_{s1}{}^{*}M_1 + V_{s2}{}^{*}M_2 + V_{s3}{}^{*}M_3 + V_{s4}{}^{*}M_4 + V_{s5}{}^{*}M_5 \\
\mathrm{L} &= \mathrm{L}_{fl}{}^{*}\varphi + L_1{}^{*}M_1 + L_2{}^{*}M_2 + L_3{}^{*}M_3 + L_4{}^{*}M_4 + L_5{}^{*}M_5 \\
1 &= \varphi + M_1 + M_2 + M_3 + M_4 + M_5
\end{aligned} \tag{A1}$$

$$\begin{pmatrix} \rho \\ AI \\ V_{\mathrm{p}} \\ V_s \\ L \\ 1 \end{pmatrix} = \begin{pmatrix} \rho_{fl} & \rho_1 & \rho_2 & \rho_3 & \rho_4 & \rho_5 \\ AI_{fl} & AI_1 & AI_2 & AI_3 & AI_4 & AI_5 \\ V_{\mathrm{p}\,fl} & V_{\mathrm{p}\,1} & V_{\mathrm{p}\,2} & V_{\mathrm{p}\,3} & V_{\mathrm{p}\,4} & V_{\mathrm{p}\,5} \\ V_{s\,fl} & V_{s\,1} & V_{s\,2} & V_{s\,3} & V_{s\,4} & V_{s\,5} \\ L_{fl} & L_{fl} & L_{fl} & L_{fl} & L_{fl} & L_{fl} \\ 1 & 1 & 1 & 1 & 1 & 1 \end{pmatrix} * \begin{pmatrix} \varphi \\ M_1 \\ M_2 \\ M_3 \\ M_4 \\ M_5 \end{pmatrix} \tag{A2}$$

where, subscript '*fl*' stands for fluid, $\phi$ is the inverted porosity, $Mi$ ($i = 1$ to 5) denotes mineral concentration of five minerals. Five minerals were selected as limestone, dolomite, quartz, shale, and heavy minerals.

The matrix system in Eq. (A3) illustrates the simultaneous matrix inversion calculation performed for mineral composition which can be expressed as

$$W = C \times M \tag{A3}$$

where, *W, C,* and *M* denote the well log measurement (i.e., the rock's physical properties), matrix of the rock constituents, and matrix of the unknown proportions of the individual mineral components, respectively. The physical properties of the dominant rock constituents used in this study for multimineral modeling are available in the literature (Singh et al., 2013). Eq. (A4) can be solved by treating it as an inverse problem and then solving for *M*:

$$M = C^{-1} \times W \tag{A4}$$

(Amosu and Sun, 2018) have developed an interactive graphical user interface program with open-source, called MinInversion. In this program, the author suggested a balanced linear model system derived from borehole geophysical logs to estimate the mineral content in a rock by an inverse method. In this particular study, we also used MinInversion to estimate mineral composition from digital geophysical logs. The MinInversion program enables the system to solve and execute the linear equation of the inversion matrix.

### *A1.2 Total and fracture porosity*

The density log was used to estimate total porosity using Eq. (A5):

$$\phi_T = \frac{\rho_{ma} - \rho_b}{\rho_{ma} - \rho_{fl}} \tag{A5}$$

where $\rho_{ma}$ and $\rho_{fl}$ denote the matrix and fluid density, respectively.

We then calculated the fracture porosity using Eq. (A6):

$$\phi_F = \frac{Frac(\phi_T - 1)}{(v\phi_T - 1)} \tag{A6}$$

where $\phi_F$ is the fracture porosity (with no vugs), *Frac* is a number of fractures, and *v* denotes the porosity partitioning coefficient.

Finally, the effective porosity ($\phi_E$) was calculated using Eq. (A7).

$$\phi_E = \phi_T(1 - V_{sh}) \tag{A7}$$

In the above equation, GR log was used to estimate the rock's shale volume ($V_{sh}$), as shown in Eq. (A8).

$$V_{sh} = \frac{GR_{log} - GR_{min}}{GR_{max} - GR_{min}} \tag{A8}$$

where $GR_{log}$ is gamma-ray reading, $GR_{min}$ and $GR_{max}$ are the minimum (clean sand) and maximum (shale) gamma-ray readings in the zone of interest, respectively.

### *A1.3 Permeability and RQI estimation*

The permeability was estimated from hydraulic flow units (HFU) as described in the following equations (Hearn et al., 1984). considered the role of the mean hydraulic radius ($r_{mh}$) for identifying and characterizing reservoir HFU. They defined mean hydraulic radius as 'the ratio between the cross-sectional area (*r*) to the wetted perimeter.

$$r_{mh} = \frac{\pi r^2}{2\pi r} = \frac{r}{2} \tag{A9}$$

The quantitative relationship between porosity and permeability as given by Darcy's laws and obtained from the Poiseuille formula can be written as,

$$K = \frac{r^2\phi}{8\tau^2} \tag{A10}$$

where *K*, $\phi$ and$\tau$ define permeability, porosity, and tortuosity, respectively. Note that $\phi$ and *K* depend on types of pores, their shape, and their connectivity. (Amaefule et al., 1993) used tortuosity (correction factor) for saturated porous media.

$$K = \frac{r^2\phi}{8\tau^2} = \frac{\phi}{2\tau^2}\left(\frac{r}{2}\right) = \frac{\phi r_{mh}^2}{2\tau^2} \tag{A11}$$

In Eq. (A11), the surface area $r_{mh}$ is expressed as per unit grain volume ($S_{vgr}$) and $\phi$, and can be defined as follows,

$$r_{mh} = \frac{1}{S_{vgr}}\left[\frac{\phi}{1-\phi}\right] \tag{A12}$$

substituting the result of $r_{mh}$ into the definition of K–C model (Amaefule et al., 1993), we arrive at the following Eq. (A13):

$$K = \frac{\phi^3}{(1-\phi)^2}\left[\frac{1}{f_g\tau^2 S_{v_{gr}}^2}\right] \tag{A13}$$

where symbol $f_g$ and $S_{vgr}$ typically represents the shape factor (dimensionless unit) and specific surface area expressed in term of grain ($\mu m^{-1}$), respectively.

In Eq. (A13), we symbolically divided $\phi$ to both sides and took a square root,

$$0.0314\sqrt{\frac{K}{\phi_e}}=\frac{\phi}{(1-\phi)}\left[\frac{1}{f_g\tau^2 S_{v_{gr}}^2}\right] \tag{A14}$$

Finally, Eq. (A14) can be expressed as:

$$RQI = FZI \times \phi_Z \tag{A15}$$

where the abbreviations *FZI* for flow zone indicator (μm) and *RQI* for reservoir quality index. $\phi_z$ is the pore volume-to-grain volume ratio.

FZI is the only property that has similar geological and petrophysical properties. According to the classical definition, FZI subdivides the reservoir into units based on flow behavior.

$$RQI = 0.0314\sqrt{\frac{K}{\phi_e}} \tag{A16}$$

where $\phi_e$ is effective porosity.

$$\phi_Z = \frac{\phi_e}{1-\phi_e} \tag{A17}$$

The value of FZI is given at the intercept of a unit-slope line with the coordinate $\phi_z = 1$ on a log-log plot (i.e., RQI versus $\phi_z$). Single value for each HFU can be identified based on FZI values.

The mean FZI ($FZI_{mean}$) values associated with the cluster was used to compute the permeability by Kozeny–Carman Eq. (A18),

$$K = 1014 \times (FZI_{mean})^2 \sqrt{\frac{\phi_e}{(1-\phi_e)^2}} \tag{A18}$$

### *A1.4 Dynamic Young's modulus*

Young's modulus (GPa) can be determined directly using shear ($V_S$) and compressional wave velocity ($V_P$) information and bulk density ($\rho_b$) (Mavko et al., 2009; Rasouli, 2012).

$$E_d = \rho_b V_s^2 \left(\frac{3V_p^2 - 4V_s^2}{V_p^2 - V_s^2}\right) \times 10^{-6} \tag{A19}$$

### *A1.5 Dynamic Poisson ratio*

The dynamic Poisson ratio can be expressed as a function of bulk modulus and shear modulus, proposed by Stein (1976).

$$\nu_d = \frac{3K - 2G}{6K + 2G} \tag{A20}$$

where $\nu_d$ denote dynamic Poisson's ratio, $K$ and $G$ are bulk modulus and shear modulus, respectively in GPa.

## References


Abdulaziz, A.M., Mahdi, H.A., Sayyouh, M.H., 2019. Prediction of reservoir quality using well logs and seismic attributes analysis with an artificial neural network: a case study from Farrud Reservoir, Al-Ghani Field, Libya. J. Appl. Geophys. 161, 239–254.

Aghli, G., Moussavi-Harami, R., Mortazavi, S., Mohammadian, R., 2019. Evaluation of new method for estimation of fracture parameters using conventional petrophysical logs and ANFIS in the carbonate heterogeneous reservoirs. J. Petrol. Sci. Eng. 172, 1092–1102.

Aghli, G., Soleimani, B., Moussavi-Harami, R., Mohammadian, R., 2016. Fractured zones detection using conventional petrophysical logs by differentiation method and its correlation with image logs. J. Petrol. Sci. Eng. 142, 152–162.

Aguilera, R., 2010. Effect of fracture dip and fracture tortuosity on petrophysical evaluation of naturally fractured reservoirs. J. Can. Petrol. Technol. 49 (9), 69–76.

Al-Ghamdi, A., Chen, B., Behmanesh, H., Qanbari, F., Aguilera, R., 2010. An improved triple porosity model for evaluation of naturally fractured reservoirs. In: Trinidad and Tobago Energy Resources Conference.

Al Moqbel, A., Wang, Y., 2011. Carbonate reservoir characterization with lithofacies clustering and porosity prediction. J. Geophys. Eng. 8 (4), 592–598.

Amaefule, J.O., Altunbay, M., Tiab, D., Kersey, D.G., Keelan, D.K., 1993. Enhanced reservoir description: using core and log data to identify hydraulic (flow) units and predict permeability in uncored intervals/wells. In: SPE Annual Technical Conference and Exhibition.

Amosu, A., Sun, Y., 2018. MinInversion: a program for petrophysical composition analysis of. Geophysical Well Log Data 8 (2), 65.

Ashraf, U., et al., 2019. Classification of reservoir facies using well log and 3D seismic attributes for prospect evaluation and field development: a case study of Sawan gas field, Pakistan. J. Petrol. Sci. Eng. 175, 338–351.

Bakhshi, E., Golsanami, N., Chen, L., 2020. Numerical modeling and lattice method for characterizing hydraulic fracture propagation: a review of the numerical, experimental, and field studies. Arch. Comput. Methods Eng. 28, 3329–3360. https://doi.org/10.1007/s11831-020-09501-6.

Boateng, C.D., Fu, L.-Y., Danuor, S.K., 2020. Characterization of complex fluvio–deltaic deposits in Northeast China using multi-modal machine learning fusion. Sci. Rep. 10 (1), 13357.

Cai, G., et al., 2008. Geochemistry of Neogene sedimentary rocks from the Jiyang basin, North China Block: the roles of grain size and clay minerals. Geochem. J. 42 (5), 381–402.

Casini, G., Hunt, D.W., Monsen, E., Bounaim, A., 2016. Fracture characterization and modeling from virtual outcrops. AAPG (Am. Assoc. Pet. Geol.) Bull. 100 (1), 41–61.

Dandan, F., Qiaodeng, H., 2002. An improved genetic algorithm and its application in parameter inversion in anisotropic media. Geophys. Prospect. Pet. 41 (3), 293–298.
Darling, T., 2005. Introduction. In: Darling, T. (Ed.), Well Logging and Formation Evaluation. Gulf Professional Publishing, Burlington, p. ix.
Dell'Aversana, P., 2019. Comparison of different Machine Learning algorithms for lithofacies classification from well logs. Boll. Geofis. Teor. Appl. 60, 69–80.
Ding, Y., Du, Q., Yasin, Q., Zhang, Q., Liu, L., 2020. Fracture prediction based on deep learning: application to a buried hill carbonate reservoir in the S area. Geophys. Prospect. Pet. 59 (2), 267–275.
Du, Q., Yasin, Q., Ismail, A., 2018. A Comparative Analysis of Artificial Neural Network and Rock Physics for the Estimation of Shear-Wave Velocity in a Highly Heterogeneous Reservoir. SEG Technical Program Expanded Abstracts 2018, pp. 2246–2250.
Du, Q., Yasin, Q., Ismail, A., Sohail, G.M., 2019. Combining classification and regression for improving shear wave velocity estimation from well logs data. J. Petrol. Sci. Eng. 182, 106260.
Esmaeilzadeh, S., et al., 2019. A General Spatio-Temporal Clustering-Based Non-local Formulation for Multiscale Modeling of Compartmentalized Reservoirs. SPE Western Regional Meeting. OnePetro.
Esmaeilzadeh, S., et al., 2020. Multiscale modeling of compartmentalized reservoirs using a hybrid clustering-based non-local approach. J. Petrol. Sci. Eng. 184, 106485.
Ferrill, D.A., et al., 2017. Mechanical stratigraphy and normal faulting. J. Struct. Geol. 94, 275–302.
Galland, O., et al., 2019. Structure, emplacement mechanism and magma-flow significance of igneous fingers – implications for sill emplacement in sedimentary basins. J. Struct. Geol. 124, 120–135.
Ge, X., Fan, Y., Zhu, X., Deng, S., Wang, Y., 2014. A method to differentiate degree of volcanic reservoir fracture development using conventional well logging data—an application of kernel principal component analysis (KPCA) and multifractal detrended fluctuation analysis (MFDFA). IEEE Journal of Selected Topics in Applied Earth Observations and Remote Sensing 7 (12), 4972–4978.
Ginting, V., Pereira, F., Presho, M., Wo, S., 2011. Application of the two-stage Markov chain Monte Carlo method for characterization of fractured reservoirs using a surrogate flow model. Comput. Geosci. 15 (4), 691.
Golsanami, N., et al., 2020. Relationships between the geomechanical parameters and Archie's coefficients of fractured carbonate reservoirs: a new insight. Energy Sources, Part A Recovery, Util. Environ. Eff. 1–25.
Golsanami, N., et al., 2019. Distinguishing fractures from matrix pores based on the practical application of rock physics inversion and NMR data: a case study from an unconventional coal reservoir in China. J. Nat. Gas Sci. Eng. 65, 145–167.
Golsanami, N., et al., 2021. NMR-based Study of the Pore Types' Contribution to the Elastic Response of the Reservoir Rock, vol. 14, p. 1513, 5.
Hearn, C.L., Ebanks Jr., W.J., Tye, R.S., Ranganathan, V., 1984. Geological factors influencing reservoir performance of the hartzog draw field, Wyoming. J. Petrol. Technol. 36 (8), 1335–1344.
Hinton, G.E., Osindero, S., Teh, Y.W., 2006. A fast learning algorithm for deep belief nets. Neural Comput. 18 (7), 1527–1554.
Hodgetts, D., et al., 2004. Three-dimensional geological models from outcrop data using digital data collection techniques: an example from the Tanqua Karoo depocentre, South Africa. Geological Society, London, Special Publications 239 (1), 57–75.
Hornby, B.E., Luthi, S.M., Plumb, R.A., 1992. Comparison of fracture apertures computed from electrical borehole scans and reflected stoneley waves: an integrated interpretation. Log. Anal. 33 (1).
Ismail, A., Yasin*, Q., Du, Q., Ahmed, A., Khan, N., 2017. Porosity-permeability Relationship in Distinct Flow Units in Light of Geophysical and Laboratory Methods, International Geophysical Conference, pp. 272–276. Qingdao, China, 17-20 April 2017.
Jun, L., Tianyao, H., Baimin, Z., 2006. Synthetic predication of favorable fracture zone from seismic and log data. Prog. Geophys. 21 (1), 179–183.
Khoshbakht, F., Azizzadeh, M., Memarian, H., Nourozi, G.H., Moallemi, S.A., 2012. Comparison of electrical image log with core in a fractured carbonate reservoir. J. Petrol. Sci. Eng. 86–87, 289–296.
Laongsakul, P., Dürrast, H., 2011. Characterization of reservoir fractures using conventional geophysical logging. Songklanakarin J. Sci. Technol. 33, 237–246.
Larssen, K., 2018. Integrated Characterization of the Upper Permian Kapp Starostin Formation in Central Spitsbergen, Svalbard. From Outcrop to Geomodel.
Lin, N., et al., 2018. Supervised learning and unsupervised learning for hydrocarbon prediction using multiwave seismic data. Geophys. Prospect. Pet. 57 (4), 601–610.
Liu, L., Tang, D., Xu, H., Liu, L., 2016. Reservoir prediction of deep-water turbidite sandstones with seismic lithofacies control —a case study in the C block of lower Congo basin. Mar. Petrol. Geol. 71, 1–11.
Loza Espejel, R., Alves, T.M., Blenkinsop, T.G., 2020. Multi-scale fracture network characterisation on carbonate platforms. J. Struct. Geol. 140, 104160.
Luo, X., Bhakta, T., Jakobsen, M., Nævdal, G., 2016. An ensemble 4D-seismic history-matching framework with sparse representation based on wavelet multiresolution analysis. SPE J. 22 (3), 985–1010.
Luo, X., Lorentzen, R.J., Bhakta, T., 2021. Accounting for model errors of rock physics models in 4D seismic history matching problems: a perspective of machine learning. J. Petrol. Sci. Eng. 196, 107961.
Martin, G.S., Wiley, R., Marfurt, K.J., 2006. Marmousi2: an elastic upgrade for Marmousi. Lead. Edge 25 (2), 156–166.
Martinez, L.P., Hughes, R., Wiggins, M., 2002. IDENTIFICATION AND CHARACTERIZATION OF NATURALLY FRACTURED RESERVOIRS USING CONVENTIONAL WELL LOGS. The University of Oklahoma, pp. 1–23.
Mavko, G., Mukerji, T., Dvorkin, J., 2009. The Rock Physics Handbook: Tools for Seismic Analysis of Porous Media. Cambridge University Press, Cambridge.
Mohebbi, A., Haghighi, M., Sahimi, M., 2007. Conventional logs for fracture detection & characterization in one of the Iranian field. In: International Petroleum Technology Conference.
Moosavi, S.R., Wood, D.A., Ahmadi, M.A., Choubineh, A., 2019. ANN-based prediction of laboratory-scale performance of CO2-foam flooding for improving oil recovery. Nat. Resour. Res. 28 (4), 1619–1637.
Movahed, Z.J.R., Amiri Bakhtiari, H., 2015. The Effect of Tar on the Petrophysical Analysis of FMI in Asmari Fractured Reservoir.
Nguyen, H., Bui, X.-N., 2019. Predicting blast-induced air overpressure: a robust artificial intelligence system based on artificial neural networks and random forest. Nat. Resour. Res. 28 (3), 893–907.
Nguyen, H., Drebenstedt, C., Bui, X.-N., Bui, D.T., 2020. Prediction of blast-induced ground vibration in an open-pit mine by a novel hybrid model based on clustering and artificial neural network. Nat. Resour. Res. 29 (2), 691–709.
Nwachukwu, A., Jeong, H., Pyrcz, M., Lake, L.W., 2018. Fast evaluation of well placements in heterogeneous reservoir models using machine learning. J. Petrol. Sci. Eng. 163, 463–475.
Ouenes, A., 2000. Practical application of fuzzy logic and neural networks to fractured reservoir characterization. Comput. Geosci. 26 (8), 953–962.
Ouenes, A., Richardson, S., Weiss, W.W., 1995. Fractured reservoir characterization and performance forecasting using geomechanics and artificial intelligence. In: SPE Annual Technical Conference and Exhibition.
Qiang, Z., Yasin, Q., Golsanami, N., Du, Q., 2020. Prediction of reservoir quality from log-core and seismic inversion analysis with an artificial neural network: a case study from the sawan gas field, Pakistan. Energies 13 (2), 486.
Rasouli, S.A.V., 2012. A log based analysis to estimate mechanical properties and in-situ stresses in A shale gas well in North perth basin. WIT Trans. Eng. Sci. 81, 163–174.
Russell, B., 2004. The Application of Multivariate Statistics and Neural Networks to the Prediction of Reservoir Parameters from Seismic Attributes.
Russell, B.H., 1988. Introduction to Seismic Inversion Methods, vol. 86.
Saboorian-Jooybari, H., Dejam, M., Chen, Z., Pourafshary, P., 2015. Fracture identification and comprehensive evaluation of the parameters by dual laterolog data. In: SPE Middle East Unconventional Resources Conference and Exhibition.
Singh, S., Qiu, F., Morgan, N., Nath, G., Pritchard, T., 2013. Critical comparative assessment of a novel approach for multi-mineral modeling in shale gas: results from an evaluation study of marcellus shale. In: SPE Unconventional Resources Conference and Exhibition-Asia Pacific.
Smith, M.W., Carrivick, J.L., Quincey, D.J., 2015. Structure from motion photogrammetry in physical geography. Prog. Phys. Geogr.: Earth Environ. 40 (2), 247–275.
Sun, Z., Lin, C., Zhu, P., Chen, J., 2018. Analysis and modeling of fluvial-reservoir petrophysical heterogeneity based on sealed coring wells and their test data, Guantao Formation, Shengli oilfield. J. Petrol. Sci. Eng. 162, 785–800.
Tao, Z., Alves, T.M., 2019. Impacts of data sampling on the interpretation of normal fault propagation and segment linkage. Tectonophysics 762, 79–96.
Temirchev, P., et al., 2020. Deep neural networks predicting oil movement in a development unit. J. Petrol. Sci. Eng. 184, 106513.
Tokhmchi, B., Memarian, H., Rezaee, M.R., 2010. Estimation of the fracture density in fractured zones using petrophysical logs. J. Petrol. Sci. Eng. 72 (1), 206–213.
Tokhmechi, B., Memarian, H., Noubari, H.A., Moshiri, B., 2009. A novel approach proposed for fractured zone detection using petrophysical logs. J. Geophys. Eng. 6 (4), 365–373.
Wu, S., Cao, J., 2016. Lithology identification method based on continuous restricted Boltzmann machine and support vector machine. Prog. Geophys. 31 (2), 821–828.
Wyllie, M.R.J., Gregory, A.R., Gardner, L.W., 1956. Elastic wave velocities IN heterogeneous and porous media. Geophysics 21 (1), 41–70.
Yasin, Q., Du, Q., Ismail, A., Ding, Y., 2018a. Identification and Characterization of Natural Fractures in Gas Shale Reservoir Using Conventional and Specialized Logging Tools, SEG Technical Program Expanded Abstracts 2018. SEG Technical Program Expanded Abstracts. Society of Exploration Geophysicists, pp. 809–813.
Yasin, Q., Du, Q., Sohail, G.M., Ismail, A., 2018b. Fracturing index-based brittleness prediction from geophysical logging data: application to Longmaxi shale. Geomechanics and Geophysics for Geo-Energy and Geo-Resources 4 (4), 301–325.
Yasin, Q., Sohail, G.M., Ding, Y., Ismail, A., Du, Q., 2020a. Estimation of petrophysical parameters from seismic inversion by combining particle swarm optimization and multilayer linear calculator. Nat. Resour. Res. 29 (5), 3291–3317.
Yasin*, Q., Du, Q., Qiang, Z., Gao, X., 2020b. Fracture Detection in Deep-Buried Carbonate Reservoir Using a Combination of Conventional Logs and Rock Physics Analysis, 2nd SEG Rock Physics Workshop: Challenges in Deep and Unconventional Oil/Gas Exploration, Qingdao, China, 25?27 October 2019. SEG Global Meeting Abstracts. Society of Exploration Geophysicists, 39-39.
Yue, D., S, W., Liu, Ji, 2007. An accurate method for anatomizing architecture of subsurface reservoir in point bar of meandering river. Acta Pet. Sin. 4.
Zhang, Y., Ruan, G., 2009. Bernoulli neural network with weights directly determined and with the number of hidden- layer neurons automatically determined. In: Yu, W., He, H., Zhang, N. (Eds.), Advances in Neural Networks – ISNN 2009. Springer Berlin Heidelberg, Berlin, Heidelberg, pp. 36–45.